Technische Universität Berlin

UNIVERSITAT POLITÈCNICA DE VALÈNCIA

Biomedical Engineering Bachelor Thesis

ANALYSIS OF THE BRAIN ATLAS' GRANULARITY INFLUENCE IN A DEEP SLEEP WHOLE-BRAIN MODEL

Author: María Lara Trullenque

Supervisor: Prof. Dr. Klaus Obermayer – Neural Information Processing Group

Co-Supervisor: Christoph Metzner – Neural Information Processing Group

Co-Supervisor: Cristiana Dimulescu – Neural Information Processing Group

Co-Supervisor: Gema Prats Boluda – Universitat Politècnica de València

Academic year: 2022-23

ACKNOWLEDGEMENTS

I would like to express my gratitude to my supervisors, Prof. Obermayer, Christoph Metzner and Cristiana Dimulescu, who offered me the possibility to carry out this project and guided me throughout it. I also wish to acknowledge the help provided by my home university supervisor, Gema Prats Boluda, who supported me and offered me help at all times. I would also like to thank my friends who have accompanied me during the process, especially Ehsan and Johann who helped me in times of code troubles. Finally, I would like to thank my family who supported me through all these years and who inspire me every day.

THESIS INDEX

ABSTRACT

Computational neuroscience is one of the most state-of-the-art disciplines for studying the human brain and its intricate mechanisms. To this aim, computational whole-brain models have become a very powerful tool. These models represent the brain as a network with a predefined number of nodes, where each node corresponds to a brain area and the connections between them are based on an empirically determined structural connectivity matrix. On this structure, a set of differential equations is used to simulate brain activity. This approach is highly useful when investigating complex brain dynamics with mathematical modeling, such as deep sleep models. In this context, the structural connectivity matrix is constructed based on an arbitrarily chosen brain atlas or parcellation. This study aims to analyze the effects of the parcellation´s granularity on a deep sleep whole-brain model. Therefore, the number of discrete brain areas is gradually increased using a local-global parcellation of the human cerebral cortex. As the brain is hierarchically organized, the resolution of the brain parcellation can be easily augmented resulting in several cortical parcellations consisting of 100, 200, and 500 parcels. In order to analyze the effects of increasing regional granularity, the model is built and run with the formerly described datasets using neurolib, a computational framework for whole-brain modeling written in Python. Its performance is then evaluated by comparing the simulated output with empirical recordings. Finally, the model analysis aims to determine what spatiotemporal patterns the model produces at different levels in order to establish whether there are significant differences between them.

Keywords: Whole-brain model; brain atlas; brain parcellation; deep sleep brain dynamics; functional connectivity

RESUMEN

La neurociencia computacional es una de las disciplinas más avanzadas para estudiar el cerebro humano y sus intrincados mecanismos. Para ello, los modelos computacionales de cerebro completo se han convertido en una herramienta muy efectiva. Dichos modelos representan el cerebro como una red con un número predefinido de nodos correspondientes a áreas cerebrales conectados entre sí en base a una matriz de conectividad estructural empírica. Sobre esta estructura, se utiliza un conjunto de ecuaciones diferenciales para simular actividad cerebral. Este enfoque es muy útil para investigar dinámicas cerebrales complejas mediante modelos matemáticos, como los modelos de sueño profundo. En este contexto, la matriz de conectividad estructural se construye en base a un atlas cerebral o parcelación cortical elegida arbitrariamente. Este estudio pretende analizar los efectos de la granularidad de la parcelación en un modelo de cerebro completo en estado de sueño profundo. Para ello, se aumenta gradualmente el número de áreas cerebrales discretas utilizando una parcelación local-global de la corteza cerebral humana. Debido a la naturaleza jerárquica de la corteza cerebral, la resolución de la parcelación cerebral puede aumentarse fácilmente, dando lugar a varias segmentaciones compuestas por 100, 200 y 500 parcelas. Para analizar los efectos del aumento de la granularidad regional, se construye el modelo y se ejecuta con los conjuntos de datos descritos anteriormente utilizando neurolib, un marco computacional para el modelado cerebral completo desarrollado en Python. A continuación, se evalúa su rendimiento comparando el resultado simulado con los registros empíricos. Por último, el análisis del modelo pretende determinar qué patrones espacio-temporales produce el modelo en los distintos niveles para establecer si existen diferencias significativas entre ellos.

Palabras clave: Modelado cerebral completo; atlas cerebral; parcelación cerebral; dinámica de sueño profundo; conectividad funcional

RESUM

La neurociència computacional és una de les disciplines més avançades per a estudiar el cervell humà i els seus intricats mecanismes. Per a això, els models computacionals de cervell complet s'han convertit en una eina molt efectiva. Aquests models representen el cervell com una xarxa amb un nombre predefinit de nodes corresponents a àrees cerebrals connectats entre si sobre la base d'una matriu de connectivitat estructural empírica. Sobre aquesta estructura, s'utilitza un conjunt d'equacions diferencials per a simular activitat cerebral. Aquest enfocament és molt útil per a investigar dinàmiques cerebrals complexes mitjançant models matemàtics, com els models de somni profund. En aquest context, la matriu de connectivitat estructural es construeix sobre la base d'un atles cerebral o parcel·lació cortical triada arbitràriament. Aquest estudi pretén analitzar els efectes de la granularitat de la parcel·lació en un model de cervell complet en estat de somni profund. Per a això, s'augmenta gradualment el nombre d'àrees cerebrals discretes utilitzant una parcel·lació local-global de l'escorça cerebral humana. A causa de la naturalesa jeràrquica de l'escorça cerebral, la resolució de la parcel·lació cerebral pot augmentar-se fàcilment, donant lloc a diverses segmentacions compostes per 100, 200 i 500 parcel·les. Per a analitzar els efectes de l'augment de la granularitat regional, es construeix el model i s'executa amb els conjunts de dades descrites anteriorment utilitzant neurolib, un marc computacional per al modelatge cerebral complet desenvolupat en Python. A continuació, s'avalua el seu rendiment comparant el resultat simulat amb els registres empírics. Finalment, l'anàlisi del model pretén determinar quins patrons espaciotemporals produeix el model en els diferents nivells per a establir si existeixen diferències significatives entre ells.

Paraules clau: Modelatge cerebral complet, atles cerebral, parcel·lació cerebral, dinàmica de somni profund, connectivitat funcional

PROJECT REPORT

Analysis of the Brain Atlas' Granularity Influence in a Deep Sleep Whole-Brain Model

Author: María Lara Trullenque

Supervisor: Prof. Dr. Klaus Obermayer – Neural Information Processing Group

Co-Supervisor: Christoph Metzner – Neural Information Processing Group

Co-Supervisor: Cristiana Dimulescu – Neural Information Processing Group

Co-Supervisor: Gema Prats Boluda – Universitat Politècnica de València

Date: 15/07/2022

Degree: Bachelor in Biomedical Engineering

UNIVERSITAT POLITÈCNICA DE VALÈNCIA

PROJECT REPORT INDEX

FIGURE INDEX

APPENDIX FIGURE INDEX

TABLE INDEX

1. INTRODUCTION

The human brain presents different types of oscillatory behavior depending on its state. During deep sleep, slow oscillations (SOs) appear and they characterize slow-wave sleep (SWS), a particular form of non-REM sleep [1]. These waves travel through the cortex generating neural activity transitions with low frequencies (<1Hz), which occur between up- and down-states where neurons are constantly firing or present almost no activity, respectively. SOs play a central role during memory consolidation [1] and are therefore an important mechanism for human life.

Oscillatory brain dynamics such as SOs are processes of a complex nature. Thus, they can be difficult to study on an empirical level, as neuroimaging methods or EEG recordings offer the possibility to observe them at a macroscopic level, but not of illustrating the underlying mechanisms. To this aim, computational whole-brain models have become a very powerful tool. These models represent the brain as a network with a predefined number of nodes, where each node corresponds to a brain area. The connections between them are based on an empirically determined structural connectivity (SC) matrix, which is derived from probabilistic diffusion tensor imaging (DTI) tractography. On this structure, a set of differential equations that compound each particular model is used to simulate brain activity, leading to firing rates of single nodes as an output. This first output can then be transformed to a simulated BOLD signal using the hemodynamic Balloon-Windkessel model [2][3]. By comparing simulated firing rates and BOLD signals to empirical recordings, electroencephalography (EEG) and resting state functional magnetic resonance imaging (fMRI) respectively, the model can be optimized and fitted to the empirical data (Figure 1).

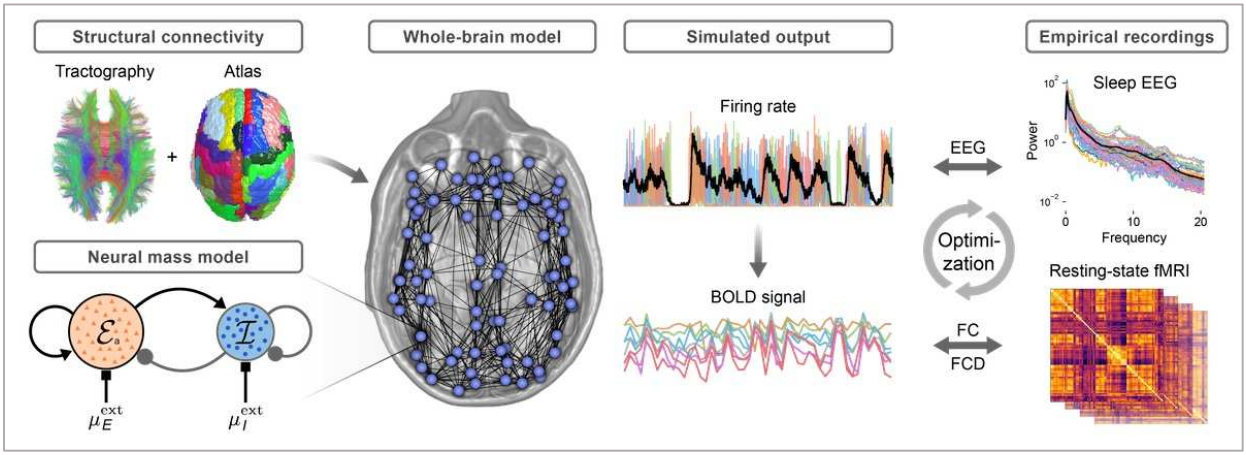

Figure 1: Structure and workflow of the whole brain model [4].

One such model, which accurately reproduces SO dynamics, is the sleep model developed in [4], where a key finding is that the connectome (defined as "the comprehensive set of neuronal connections of a species' central nervous system" [5]) shapes the oscillatory dynamics. In the particular case of SOs, they travel from frontal to posterior regions as waves of silence [4]. This behavior is correlated with the node's degree, which describes the sum of connections of a single node [6]. The regions with lower node degree are more likely to change into a non-activation state

(down-state) given the fact that they receive less excitatory input from other nodes. In this context, the role of the structural connectivity matrix is crucial, because it establishes the node degree by describing the internodal connections.

When building the model, the SC matrix is based on an arbitrarily chosen brain atlas or parcellation. This study aims to analyze the effects of the parcellation´s granularity on a deep sleep whole-brain model. Therefore, the number of discrete brain areas is gradually increased using the local-global parcellation of the human cerebral cortex [7]. As the brain is hierarchically organized, the resolution of the brain parcellation can be easily augmented, resulting in several cortical parcellations consisting of 100, 200, and 500 parcels. Granularity is, in general, an interesting aspect to take into account, given the fact that most connections in the human brain are less than 50mm apart, but there is no consensus on which granularity level is more adequate to simulate and study concrete brain dynamics, such as SOs. Roberts et. al [8] analyzed wave propagation patterns with a high resolution parcellation (513 brain areas were considered) based on the idea that these global oscillations are generated due to local interactions, which could be missed with coarser grained parcellations. On the other hand, Cakan et al. [9] used lower levels of resolution (80 nodes) to study spatiotemporal patterns, suggesting that high granularity is not a necessary condition for the formation and propagation of such waves. Consequently, the question addressed in this study is whether finer parcellation schemes offer the possibility to observe additional characteristics underlying the dynamics of SOs. Additionally, some studies show that the selection of the brain atlas influences the model's outcomes [10]. All in all, the choice of the brain parcellation is not trivial and could lead to different results depending on the implementation.

In order to analyze the effects of increasing regional granularity, the model is built and run with the formerly described datasets using Neurolib [2], a computational framework for whole-brain modeling written in Python. The study procedure starts with a state space analysis which aims to establish the model's state with different parameter selection throughout all different levels of resolutions. This way, it can be seen whether the appearing states are maintained while increasing regional resolution. Secondly, oscillatory spatiotemporal patterns are observed at different granularity levels and the model's performance is evaluated by comparing the simulated output with empirical recordings. Finally, a more concrete case of parameter selection is chosen from the work of Cakan et al. "*Spatiotemporal Patterns of Adaptation-Induced Slow Oscillations in a Whole-Brain Model of Slow-Wave Sleep*" [9]. In this study, an evolutionary optimization was run in order to find the optimal parameter selection for a deep sleep model. Now, this work aims to use the same obtained optimal parameter values for reproducing the results of Cakan et al. with different resolution levels and investigate whether there are significant differences in spatiotemporal patterns, as well as in the statistical properties of the simulated outputs.

2. THEORETICAL FRAMEWORK

There are two basic states of sleep in mammals: rapid-eye-movement (REM) sleep and non-REM sleep. Both appear as different phases which alternate during the whole sleep process. While REM sleep presents a more awake-like state of the brain, SOs appear during SWS, which is part of non-REM sleep and travel through the cortex, generating high-amplitude waves in the local field potential. These waves are generated locally, but spread as global waves of silence through the brain cortex [4]. The travelling direction is determined by the brain connectome, which is heterogeneously structured, causing SOs to propagate with a preferred direction from anterior to posterior brain areas [4].

The different kinds of neural stages during sleep are associated with consolidation processes for different types of memories. In the SWS case, it is assumed that it serves in declarative memory consolidation. In this context, the Active System Consolidation Hypothesis establishes that newly obtained memories are reactivated during SWS, a mechanism that allows them to transfer from a temporary (hippocampus) to a long-term (neocortex) storage site [1]. SOs are able to reach hippocampal memory units through a top-down control over subjacent oscillation processes with lower amplitude, specifically thalamo-cortical spindles and hippocampal ripples. These smaller and faster oscillations combine forming spindle-ripple events which serve to the reactivation of memory representations (Figure 2).

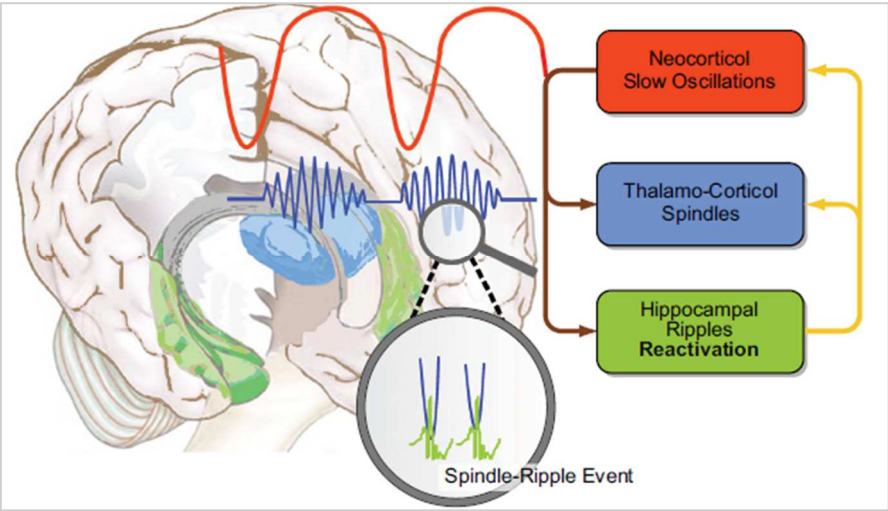

Figure 2: Model of the active system consolidation during sleep [1].

The reactivation of memory trace areas during sleep can be observed through brain activation imaging techniques, such as functional magnetic resonance (fMRI) or positron emission tomography (PET). Several studies showed clear signs of reactivation of memory related areas (hippocampal and parahippocampal regions) in humans during SWS after a hippocampus-dependent learning process. This was achieved through, for example, evaluating neural reactivation after a spatial learning task taking regional cerebral blood flow (rCBF) as an activity marker [11]. In addition, similar levels of enhanced EEG coherence (which describes the correspondence in the neural activation patterns between two or more brain regions) were found

while carrying out a word-learning task and during the following SWS [12]. These results are coherent with the Active System Consolidation Hypothesis and therefore support the role of SOs as a higher level phenomenon in control of spindle-ripple events, which mediate the hippocampo-neocortical interaction leading to memory consolidation.

However, even though the reactivation of memory related brain areas can be observed using the former mentioned imaging techniques, computational modelling is a useful approach for their characterization as it offers a mechanistic understanding of the underlying processes and gives us the possibility of exploring a wide range of parameters. In the case of SWS, there are studies showing the appropriateness of implementing whole brain models in order to analyze this kind of brain dynamics [4]. This approach is highly convenient to gain a deeper understanding of the phenomena occurring during SWS as it is based on structural and functional connectivity data which play a crucial role when it comes to travelling waves such as SOs.

3. PROJECT OBJECTIVES

The goals of this project are, firstly and from a more general perspective, to gain a deeper understanding on the role of the atlas parcellation in whole-brain modelling. More concretely, this study aims to prove whether there are significant differences in the state of the model, as well as in the appearing spatiotemporal patterns and statistics when the level of resolution is increased. This way, the importance of having consistent results with the different parcellations can be enlightened, as this aspect should be taken into account when comparing results with different model constructions.

4. METHODS AND MATERIALS

4.1. Empirical Data

The empirical data used in this study is the same as in the work of Cakan et al. [9], where all specific parameters from the acquisition and preprocessing techniques are presented in detail. Structural and resting-state fMRI data were acquired from a group of 27 older adults at the Universitätsmedizin Greifswald. Both structural and functional data were obtained using the same system, a 3T Siemens MAGNETOM Verio Syngo b17 MR scanner.

Firstly, the structural image data was acquired through high-resolution anatomical T1 images. On the other hand, for diffusion data, the images were obtained with a single-shot echo-planar imaging (EPI) sequence. In both cases, the preprocessing consisted in segmentation of the brain and artifact removal carried out using a semi-automated pipeline implemented in the FSL toolbox, a comprehensive library of analysis tools for MRI, fMRI and DTI data [13]. The latter is a technique which offers the possibility to obtain the anatomical structure of the brain connectome through probabilistic tractography. More concretely, probabilistic tractography estimates the pathways that originate at any given seed voxel based on intra-voxel crossing fibers and provides quantitative information about the probability of structural connectivity that a white matter tract will pass through any other voxel in the brain [14] . In order to compute the structural connectivity matrices from the probabilistic tractography data, every connection strength C between two areas i and j was calculated as the average between the connection strength C_{ij} and C_{ji}, so that the SC matrix is symmetrical. Furthermore, connectivity matrices were normalized by dividing every entry by the maximum connectivity value so that all entries were in the range [0;1]. Nevertheless, the construction of the model was based on a single structural connectivity matrix which consisted on the average of all the subject-specific matrices. The obtained connectivity value between every two regions is multiplied by a coupling strength parameter (K_{gl}) in order to determine every specific coupling strength. The fiber length matrix was also obtained through averaging every individual fiber length matrix and in this case, the matrix entries are divided by the signal propagation speed value (v_{gl}) to form a time-delay matrix [9].

The resting state fMRI images were attained by scanning the participants during 12 minutes with TR = 2000ms and TE = 30ms, and data preprocessing was conducted using the FEAT toolbox [9], a software toolbox for high quality model-based fMRI data analysis [8]. This way, artifacts and non-brain tissue were removed and the fMRI images were linearly registered to each subject's anatomical data. Finally, for every brain region, the average BOLD time series was calculated [9].

4.2. The local-global parcellation of the human brain cortex

The human brain cortex has been traditionally subdivided into several brain areas, following the idea that every cortical area serves a different function and presents its particular architecture and connectivity patterns [15]. However, as the brain is hierarchically organized, each area can potentially be subdivided into smaller parcels. For instance, the motor cortex presents intra-areal heterogeneities, given the fact that the different body parts are represented as distinct

neurobiological units [16]. Functional neuroimaging techniques such as fMRI or PET are powerful non-invasive tools which allow to distinguish different brain areas and even subareal parcellations [17]. The latter seem to be captured when implementing resting-state fMRI (rs-fMRI), an imaging technique which offers the possibility to obtain resting-state functional connectivity (RSFC) data. RSFC measures the synchronization of rs-fMRI time series between different brain areas and is therefore not a direct insight of anatomical connectivity. Nevertheless, RSFC reflects the organization of large-scale task-evoked circuits as it is delimited by anatomical constraints [18].

The challenge of parcellating the brain through rs-fMRI has been faced through two different major approaches: the local gradient and the global similarity approach. On the one hand, the local gradient method delimits the parcels by detecting abrupt changes in RSFC patterns, which are understood as borders between different areas [19]. Some studies show, that the results obtained following the local gradient approach are similar to histological delineation of cortical areas [19]. On the other hand, the global similarity method exploits the idea that one brain area is associated to a specific function. Therefore, it clusters regions with similar rs-fMRI signals or RSFC patterns regardless of spatial proximity [20]. All in all, while the local gradient approach distinguishes areas with high intra-areal homogeneity [21], the global similarity approach differentiates parcels which are homogeneously connected [22]. Taking into account the strengths that the different approaches present, the option of integrating them can be seen as a solution in order to generate parcellations that are not only homogeneous internally, but also regarding the connectivity aspects.

Following this idea, Schaefer et al. [7] developed a gradient-weighted Markov Random Field (gwMRF) model that combines the local gradient and global similarity approach, generating the local-global parcellation of the human cerebral cortex [7]. The concept behind the model is the following: a balance is found between a global similarity objective, which clusters voxels with similar T1 intensities, and a local smoothness objective, which encourages adjacent voxels to be labeled the same if the local RSFC gradient is low [7]. This way, a good compromise is reached between functional and connectional homogeneity, and architectonic boundaries. In addition, different levels of parcel resolution can be achieved by subdividing regions, therefore, in this study parcellations of 100, 200 and 500 areas are implemented.

Overall, the choice of a parcellation when studying the brain plays a crucial role, because it offers the possibility to reduce dimensionality, as working with the data at voxel level resolution is problematic due to the amount of computational resources that would be required and the inefficiency this would generate. However, dimensionality reduction has to maintain the characteristics of the studied data and therefore, in this case, the local-global parcellation (also known as Schaefer parcellation [7]) is an appropriate approach to be faithful both to histological and connectivity features of the acquired images.

4.3. The ALN model

4.3.1. Neural-Mass Model

Each cortical region consists of a neural mass model, which attempt to model the dynamics of a large number of neurons clustered as one brain region [23]. The current modelling framework implements graph theory by representing the brain as a network of nodes (one for each brain area) interconnected by edges. This is an appropriate approach when dealing with a vast population of neurons, because working at single neuron level is computationally not efficient. The mass model is built by applying mean-field theory to populations of excitatory and inhibitory neurons. This means, in order to study the behavior of a high-dimensional system, a simpler approximated model is generated by averaging over the activity of the neurons in the populations [24]. In other words, instead of having one activity variable for each neuron in the network, there is one activity variable for an entire population of identical neurons. This way, the degrees of freedom are reduced considerably.

The considered neuron model is an adaptive exponential integrate-and-fire (AdEx) model [25], which reproduces the sub- and supra-threshold voltage traces of pyramidal neurons from cerebral cortex successfully [26]. In this approach, an exponential spike mechanism is combined with an adaptation equation in order to simulate neural activity [27]. In general, the dimensionality reduction reached through the neural-mass model offers the possibility to simulate and analyze a brain model in a faster and more efficient way. Moreover, the mean-field neural mass model has been previously validated against higher resolution spiking neural networks [25].

Regarding the excitatory and inhibitory populations, a delay-coupling mechanism connects both of them and the excitatory population is also equipped with a somatic adaptation feedback mechanism. The populations and the links between them are illustrated in Figure 3, where the excitatory population is represented in red (ε_a) and the inhibitory population (I) in blue. The subpopulations are connected via a delay-coupling mechanism and a somatic adaptation feedback coming from the excitatory subpopulation. The latter is activity dependent, which means that in a high-activation regime, it leads to hyperpolarizing currents that destabilize the neurons in the up-state causing a fall into the down-state [9]. On the other hand, in a low-activation state, the inhibitory adaptation currents will decrease (with a specific timescale τ_α) until the current excitatory input is strong enough to drive the system back to the up-state. This balance causes a slow oscillation between up and down-states [9]. The adaptation mechanism is governed by the adaptation strength parameter b. Also, both instances receive external input currents μ^{ext} with a standard deviation σ^{ext}.

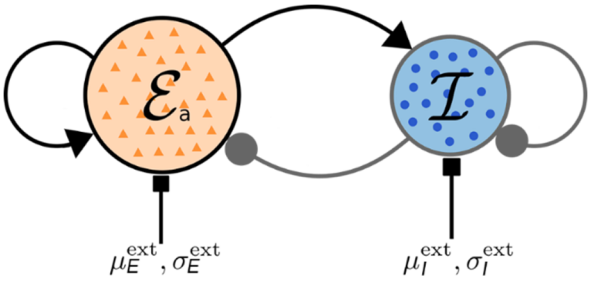

Figure 3: Composition of the ALN model [26].

4.3.2. Model Equations

In this section, the equations from the linear-nonlinear cascade model used for defining each node's dynamics in the whole brain model simulations are presented. A more detailed mathematical derivation of the model's equations is provided in the references [28] [25] and underlying dynamical mathematical descriptions such as those for synaptic currents are presented in the work of Cakan et al. [9].

The steady-state and transient dynamics of each population can be determined by solving a set of ordinary differential equations defined by a low-dimensional linear-nonlinear cascade model [24], [25]. The parameters appearing in the equations are summarized in [9] Table 1. Each brain region is represented by a node formed by two subpopulations: excitatory (E) and inhibitory (I) populations, so $\alpha \in \{E, I\}$. The following equations establish the dynamics of every node:

$$\tau_\alpha \frac{d\mu_\alpha}{dt} = \mu_a^{syn}(t) + \mu_a^{ext}(t) + \mu_a^{ou}(t) - \mu_\alpha(t) \tag{1}$$

$$\mu_a^{syn}(t) = J_{\alpha E}\bar{s}_{\alpha E}(t) + J_{\alpha I}\bar{s}_{\alpha I}(t) \tag{2}$$

$$\sigma_\alpha^2(t) = \sum_{\beta \in \{E,I\}} \frac{2J_{\alpha\beta}^2\, \sigma_{S,\alpha\beta}^2(t)\, \tau_{S,\beta}\, \tau_m}{\left(1 + r_{\alpha\beta}(t)\right) \tau_m + \tau_{S,\beta}} + \sigma_{ext,\alpha}^2 \tag{3}$$

The first equation (1) describes the dynamics of the total membrane current μ_a, which are defined by the incoming synaptic (μ_a^{syn}) and external input currents (μ_a^{ext}) as well as by the external noise contribution (μ_a^{ou}). Here, the considered means and also variances are for all neurons inside of a population. Secondly, the synaptic current is defined by the parameters $J_{\alpha\beta}$, which describe the maximum synaptic current coming from a completely active population α to β or vice versa (2). In the third equation (3) the variance of the membrane currents σ_α^2 is calculated taking into account the synaptic parameter $J_{\alpha\beta}$, other variances such as the synaptic variance ($\sigma_{S,\alpha\beta}^2$) and the external input variance ($\sigma_{ext,\alpha}^2$) as well as the involved time constants, $\tau_{S,\beta}$ for synaptic phenomena and τ_m for membrane dynamics. The parameter $r_{\alpha\beta}$ represents the mean effective input rate from population β to α and occurs under a specific transition delay. Its mathematical definition contains the parameters K_{gl} as the global coupling strength, C_{ij} as a connection measure between regions i and j and D_{ij} as elements from the fiber length delay matrix. The detailed definition of $r_{\alpha\beta}$ dynamics is presented in the references [9].

Moreover, precomputed transfer functions are implemented at every time step to define the input-dependent adaptive timescale τ_α, the population's instantaneous spike rate r_α and mean membrane potential $\bar{V}_E$ ($\phi_{r,\tau,V}(\mu_a, \sigma_a)$,).

Finally, the mathematical definition of the adaptation currents is presented as follows:

$$\frac{d\bar{I}_A}{dt} = \tau_A^{-1}(a(\bar{V}_E(t) - E_A) - \bar{I}_A) + b \cdot r_E(t) \qquad (4)$$

In (4), an adiabatic approximation is used to define the mean adaptation currents in terms of the firing rate r_E of the population [9]. The adaptation current acts as an inhibitory mechanism and its dynamics are slower compared to the membrane currents. However, in the study of Cakan et al. and therefore in this one as well, the adaptation current is only defined by the finite spike-triggered adaptation parameter b [9] while the the adaptation parameter a is set to 0. The reason of setting a to 0 is mainly because no new states appeared with a finite a compared to when only b was varying [25].

4.4. Neurolib

In this study, all simulations and analysis procedures are carried out using Neurolib, a simulation framework for whole brain neural-mass modeling written in Python. In general, the computational framework allows the user to load structural and functional datasets in order to build the model, manage the model's parameters, perform simulations and store their outputs in for further analysis. Moreover, other functionalities can be used to optimize the model comparing the outputs against empirical data. In Figure 4, the framework architecture is presented in a schematic way. A detailed description of the library can be found in the references [2] as well as at https://github.com/neurolibdev/neurolib.

Following the presented structure, in this work the class *Dataset* is used in order to handle the empirical data, which is then used to build and simulate the model through the *Model* class. For the state-space exploration, the *BoxSearch* class is implemented, and this way a parameter box search for a given model and a range of parameters is performed. Finally, Neurolib's postprocessing functions are used in the in further analysis sections in order to study the appearing spatiotemporal patterns and reproduce several figures from the work of Cakan et al.

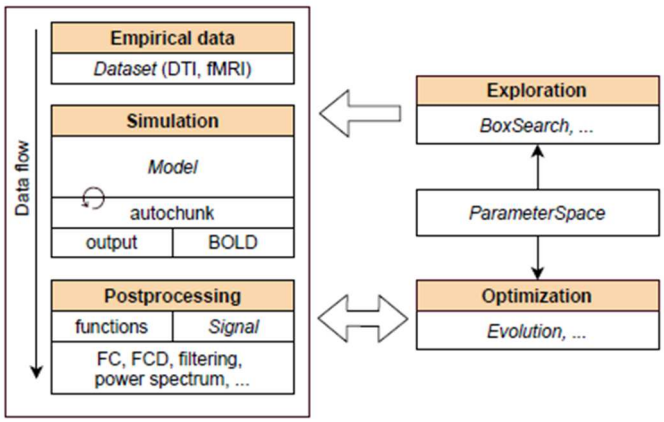

Figure 4: Neurolib Framework architecture [2].

4.5. State Space Analysis

The analysis in this current study starts with a parameter exploration in which the behavior of the system is observed when the mean input currents to the excitatory (μ_E^{ext}) and inhibitory (μ_I^{ext}) populations are changed. The rest of the parameters are taken from the exploration in [9] ($K_{gl} = 200, \tau_A = 600ms$) . More concretely, the input currents vary from 0.0 to 4.0 in 51 steps and the maximum excitatory rate of the system, as well as the dominant frequency of each node are measured. The goal is to establish the state of the model for different parameter configurations. In order to do so, the model is run for 30s for every point in the diagram, leading to a total of 51 x 51 simulations for the whole-brain network, where every simulation is initialized randomly and carried out without adding external noise ($\sigma_{ou} = 0\ mV * ms^{-3/2}$). Moreover, the state space diagrams are computed without adaptation ($b = 0pA$) and with adaptation ($b = 20pA$).

When plotting the results of the exploration as bifurcation diagrams, the bifurcation points of the system are marked through transition lines which separate the different states. These were defined by thresholding different measures in the output of the model in order to classify the state. Following this idea, the model can occupy one of four states: up, down, bi-stable or oscillatory.

Firstly, the up- and down-states are stable states in which the network is either firing or silent, respectively. Secondly, the bi-stable state is defined as a non-oscillatory regime in which a node can be pushed from a stable down-state to a stable up-state with an external stimulus or vice versa. In order to classify a point as bi-stable, a decaying stimulus first in the negative and then in the positive direction is applied to the excitatory population of every node. Therefore, if a node was in the bi-stable regime, it would fall to the down-state and subsequently jump to the up-state as a result of the stimulus. The state of the model is defined as bi-stable if after the stimulus had dropped to 0 (after 8s) a difference in the mean firing rate in any brain area of at least 10Hz was detected. For this measure, the mean firing rate is calculated in a 2s time window. The 10Hz threshold was established in the work of Cakan et al. as it was "less than the smallest difference in firing rate between any down- and up-state in the state space" [9].

Continuing with the oscillatory regions, they were classified as such when the oscillation amplitude of the firing rate was larger than 10Hz in at least one brain area. The 10Hz threshold is again taken from the work of Cakan et al. as "all oscillatory states had a larger amplitude across the entire state space" [9]. This establishes the limit for the amplitude of the firing rate oscillation, ergo the differences in the appearing firing frequencies, which is not to be confused with the actual frequency in which one node is firing. On the other hand, the criterion of classifying a point in the diagram as oscillatory if at least one single node of the whole network is on oscillatory regime is based on the fact that the regions in which state transitions from stable to oscillatory states occur gradually for each brain area can be disregarded in the analysis as they are very narrow [9].

Two different oscillatory states can be observed, a fast and a slow limit cycle (LC). On the one hand, the fast oscillations are generated by the coupling of excitatory and inhibitory populations and characterized by a range of frequencies between 15 and 35 Hz [9]. On the other hand, the slow limit cycle arises from the destabilization of the bi-stable state due to the adaptation mechanism.

This generates slow oscillations with frequencies around 0.5-2Hz [9]. This phenomenon will be explained in detail in the results section.

4.6. Spatiotemporal Analysis

The goal of the spatiotemporal analysis is to investigate whether the appearing dynamical patterns vary when the regional resolution is increased. Therefore, the measurement of the interhemispheric synchrony will be implemented. This is a measure that allows to identify different states and transitions in the model. Here, the travelling SOs can be identified as regions of high synchrony which occur when the silent wave is spreading and many areas remain inactive at the same time.

In order to compute the interhemispheric synchrony, the intrahemispheric coherence has to be calculated first. This is a quantification of the instantaneous coherence in the activation patterns of the nodes within a hemisphere. Using the Hilbert phase $\phi j(t)$ at each node *j*, the coherence for a set of nodes S is calculated in terms of an order parameter $R_S(t)$ [8], given by (5).

$$R_s(t) = \frac{1}{|S|}\left|\sum_{j \in S} e^{i\Phi_j(t)}\right| \qquad (5)$$

This measure is calculated for both right and left hemispheres. Next, the interhemispheric synchrony is defined as the sliding-window time-lagged cross-correlation between the two measures of intrahemispheric coherence. This measure is time-dependent (via the windowing) and it also depends on the cross-correlation lag. Here, a window of 100ms with 90% overlap is used, as this allows for an increase in the smoothing at the expense of temporal resolution [8].

Apart from the cross-correlation, the rate time-series (the raw output of the model) for the whole network is plotted for 20s in order to observe the activation patterns occurring during SOs. Moreover, the power spectra at the different resolution levels are computed o observe the spectral distribution of the appearing temporal patterns.

Finally, in order to compare the obtained results at different levels of resolution with the empirical data, the simulated FC matrices are computed and compared to the empirical FC matrices. The simulated FC matrices are obtained via the simulated BOLD signal, which is governed by a set of differential equations that shape the hemodynamic response of a brain area to neural activity [2]. The simulated BOLD signal is obtained from the output of the model by applying a hemodynamic Balloon-Windkessel model [2][3]. In order to match the rate of fMRI recordings, the simulated BOLD signal is subsampled at 0.5Hz after numerical integration [2]. After that, it is possible to extract a simulated FC matrix through the Pearson correlation of the simulated BOLD signal between the different nodes. This simulated FC matrix is compared to the empirical one and correlation values are obtained (Pearson correlation of the lower triagonal of the two matrices) to quantify the fitting of the model to the empirical data. Note that for computing the simulated FC matrix, the first 5 volumes of the BOLD signal are eliminated as a transient to avoid artifacts. This correlation values between empirical and simulated FCs are then compared to the correlation

values between empirical FC and SC matrices, following the idea that structural connectivity alone explains a certain portion of the variance in the functional connectivity, but having an optimal model for the microcircuit can lead to explain a larger portion of this variance through the simulated FC matrix.

4.7. Analysis of the atlas granularity's influence when reproducing results from the work of Cakan et al. [9]

In the work of Cakan et. al [9], spatiotemporal patterns and statistical measurements in a whole-brain model of slow-wave sleep are analyzed. To this aim, the brain was parceled using the automatic anatomical labeling (AAL2) atlas defined in [29]. Hereby, they obtained 80 cortical regions. In this study, these results will be compared to the ones obtained with the local-global parcellation of the human brain [7] and higher levels of resolution. Note that, in the work of Cakan et al. [9], the model was fitted to the empirical data through an evolutionary optimization algorithm in order to perform the analysis in a point where the empirical data were reflected as accurately as possible. In this work, no optimization process was carried out. Instead, the same parameter values as in [9] was selected ($\mu_E^{ext} = 3.3\, mV * ms^{-1}, \mu_I^{ext} = 3.7 mV * ms^{-1}$, $b = 3.2pA, \tau_A = 4765ms$, $K_{gl} = 265, \sigma_{ou} = 0.37 mV * ms^{-3/2}$) so that it could be proven, whether the optimal parameter values remain the same when changing the parcellation scheme. As the simulation with the chosen parameter values showed different results as in [9], an exploration around this point was performed (varying b and τ_A) in order to obtain three points (one for each level of resolution) that were equivalent to the one analyzed in [9]. Parameters b and τ_A were selected for the exploration because, firstly, as the resolution level is increased, the adaptation parameter b may be increased as there are more regions that also have greater influence in each other in terms of adaptation (as the distance between them is smaller). In the cae of τ_A, the adaptation time constant, it was also varied as it also plays a role in the adaptation mechanism, which shapes the spatial pattern of slow-wave activity [9]. The equivalent points were evaluated in terms of frequency distribution (comparison of the power spectra with the one from the work of Cakan et al. [9] and the empirical power spectrum) and also by comparing the state plots, which will be explained below.

In the reproduction of the figures in [9], firstly, the up- and down-states are detected by thresholding the firing rate of every brain area in a similar way to other studies [30],[31]. One region will be considered to be in the up-state if at any time t, its instantaneous firing rate is higher than the threshold $r_E(t) > 0.01 * \max(r_E(t))$. If this does not apply, the region will be considered to be in the down-state. Also, states with a shorter duration than 50ms were replaced by the preceding state. The state measure was conducted both for 1 min and 10 min, and the latter were used to compute further statistics, so that a high level of robustness was ensured. The states plots were also compared to the firing rate averaged across all nodes in the network, in order to see how the defined state is reflected in it. In addition, the wave propagation through the cortex was observed by selecting the time of a well-defined down-state in the states plot and analyzing the state of the nodes shortly before and after this time instant.

On the other hand, for the analyzed statistics, some other measurements are calculated. Firstly, the node's degree defines the level of connection from one node to the others. For one node i, the degree is computed as the sum of the $i-$ row in the FC matrix and normalized by dividing it by the maximum value in the sum of the rows in the FC matrix. This way, the degree value will be in the interval [0,1].

Moreover, the involvement time series $I(t)$ is calculated as a fraction of the number of brain areas n in a given time t divided by the total number of nodes N. This measure is defined in the work of Cakan et al. [9] and previously in other studies as [32]. In this study, if not stated differently, the involvement in the down-state will be considered, as in [9]. Furthermore, a distinction between global and local waves is done based on the involvement time series. Therefore, a peak finding algorithm is implemented as explained in [9]. Oscillations are considered global if the amplitude in the involvement time series was larger than 50%, otherwise, when $25\% < I(t) < 50\%$ the phenomena are considered local, while oscillations with less than 25% involvement are discarded [9]. Note that this classification thresholds are taken from [32].

Furthermore, other statistics are based on the whole-brain oscillation phase. In order to determine the mean phase of up- and down-state transitions for the global oscillations in every brain area, the global phase ($\phi(t)$) of SOs is computed via the Hilbert transform of the down-state involvement time series [9]. After bandpass filtering the $I(t)$ signal as indicated in [9], it is converted to a complex-valued time series $R(t) = A(t)\exp(i\phi(t))$ and this phase $\phi(t)$ from $R(t)$ is used as the phase for the whole-brain oscillations [9].

Once all measures and statistics are computed, a comparison between them is performed throughout the different levels of resolutions.

5. RESULTS

5.1. Results of the State Space Analysis

Figure 5 shows the bifurcation diagrams of the whole-brain network for the different levels of resolutions with and without adaptation as a result of the state space analysis. Bifurcation diagrams of the whole-brain network are computed without adaptation ($b = 0pA$) and with adaptation ($b = 20pA$) across the different levels of resolution (100, 200 and 500 nodes). Horizontal and vertical axes indicate the mean input current to the excitatory (μ_E^{ext}) and inhibitory (μ_I^{ext}) population respectively. Both input currents vary in the interval [0,4] in 51 steps. Stable states are denoted as "up" and "down", whereas the bi-stable region is marked in a dashed green contour and indicated by "bi". White contours cover the limit cycles, LC_{EI} (fast limit cycle) and LC_{EA} (slow limit cycle). Parameters are $K_{gl} = 200, \tau_A = 600ms, \sigma_{ou} = 0mV * ms^{-1}$(all other parameters are given in [9] Table 1). At first glance it can be seen that the state space of the model is not affected by the granularity increment as the appearing states remain constant in the parameter space both with and without adaptation.

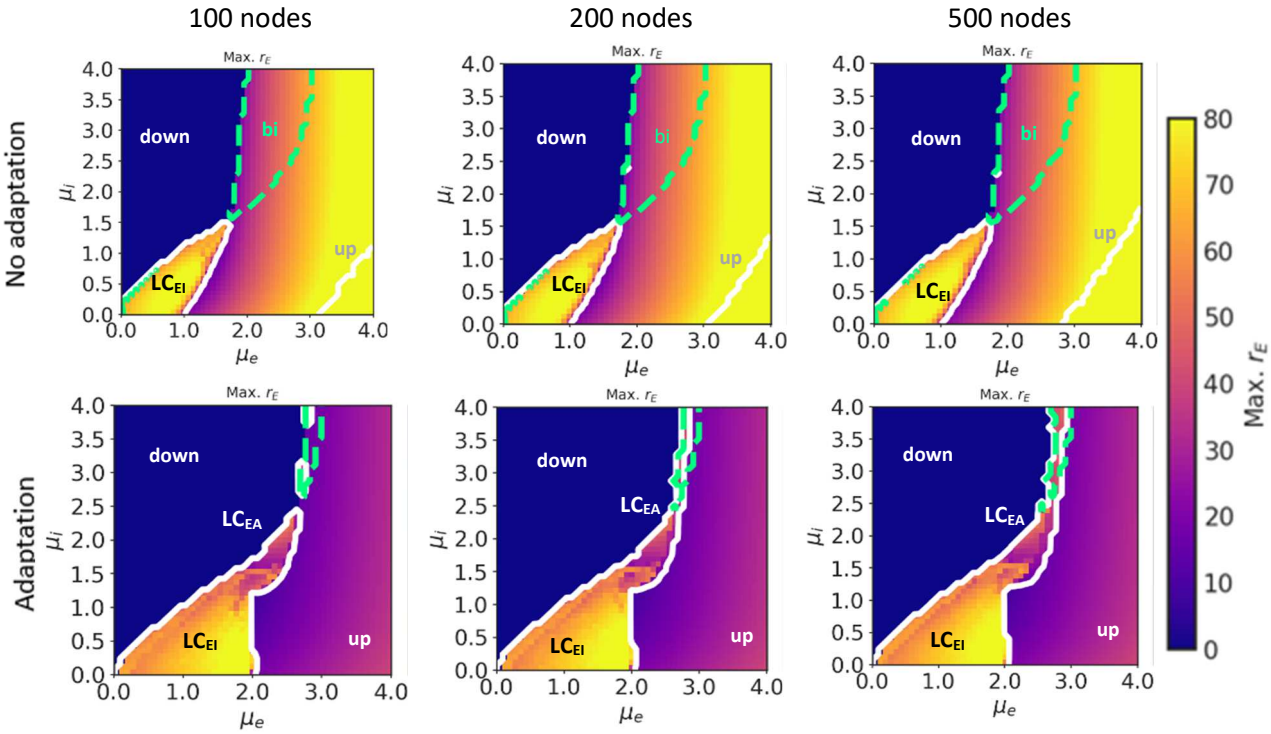

Figure 5: State space of the brain network.

On the one hand, without adaptation, the model's dynamics show different states depending on the mean external input currents. There are two stable states, a down-state, where the network shows almost no activity and an up-state, in which an asynchronous firing in the microscopic level leads to a constant high firing rate [25]. These two stable states coexist in the bi-stable region marked with dashed green lines in the diagrams. In addition, a fast limit cycle (LC_{EI}) can be found in which the coupling of the excitatory and inhibitory subpopulations shows oscillations with frequencies between 15-35Hz. Note that there seems to be a numerical artifact appearing as a mark of a limit circle in the right bottom corner of the diagrams. To prove that there is no limit circle arising in this region, some firing rates of the model with the parameter selection leading to the abnormal limit circle were plotted. The plots (see Supplementary Figure 1 in appendix) showed this point as a normal up-state suggesting that there was some numerical artifact and no real limit circle is generated in that region.

On the other hand, the bifurcation diagrams from the model with adaptation (Figure 5 , bottom row) which also remain constant throughout the different levels of resolution, show how the bi-stable region is replaced with another limit cycle LC_{EA} due to the activity-dependent adaptation mechanism. The hyperpolarizing currents triggered by the adaptation mechanism destabilize the nodes in the up-state in the bi-stable region and they decay to the down-state. Here, the inhibitory adaptation currents decrease (as they are activity dependent) and therefore, when the excitatory input is strong enough, the system jumps to the up-state again. All in all, this phenomenon (controlled by the adaptation parameter b) generates a slow oscillation with frequencies around 0.5-2Hz. This area where slow oscillations appear will be the region of interest for the spatiotemporal analysis.

For the spatiotemporal analysis, the region of interest was the slow limit cycle (LC_{EA}), so the following results are for the parameter selection $\mu_E^{ext} = 2.5$ and $\mu_I^{ext} = 2.0$ where the dominant oscillation frequency is 1Hz (the rest of the parameters remain as specified in Figure 5).

5.2. Results of the Spatiotemporal Analysis

Figure 6 shows the results for the interhemispheric synchrony and the rates at the different granularity levels. As mentioned before, the parameter selection is $\mu_E^{ext} = 2.5$ and $\mu_I^{ext} = 2.0$ and the rest of them remain as in Figure 5. Firstly, when analyzing the interhemispheric synchrony, it can be observed that there are clearly marked instants of time (every 1s approximately) where the value of the cross-correlation between both hemispheres is very high. This pattern appears through all different parcellations for the selected point and represents the spreading of SOs, where the silent wave travelling through the cortex generates great levels of coherence between the nodes. Hence, at least for this parameter combination, increasing the granularity does not lead to the emergence of new patterns observable in the interhemispheric synchrony. Moreover, this phenomenon can be observed in the firing rate plots, where nodes show higher firing rates also every 1s approximately and in great synchrony. The 1Hz dominant frequency of the spreading waves can also be observed in the power spectra which are added in the appendix (Supplementary

Figure 2). However, in the rate plots, there is a small, but discernible difference, with onset and offset of up-states more desynchronized as the granularity is increased.

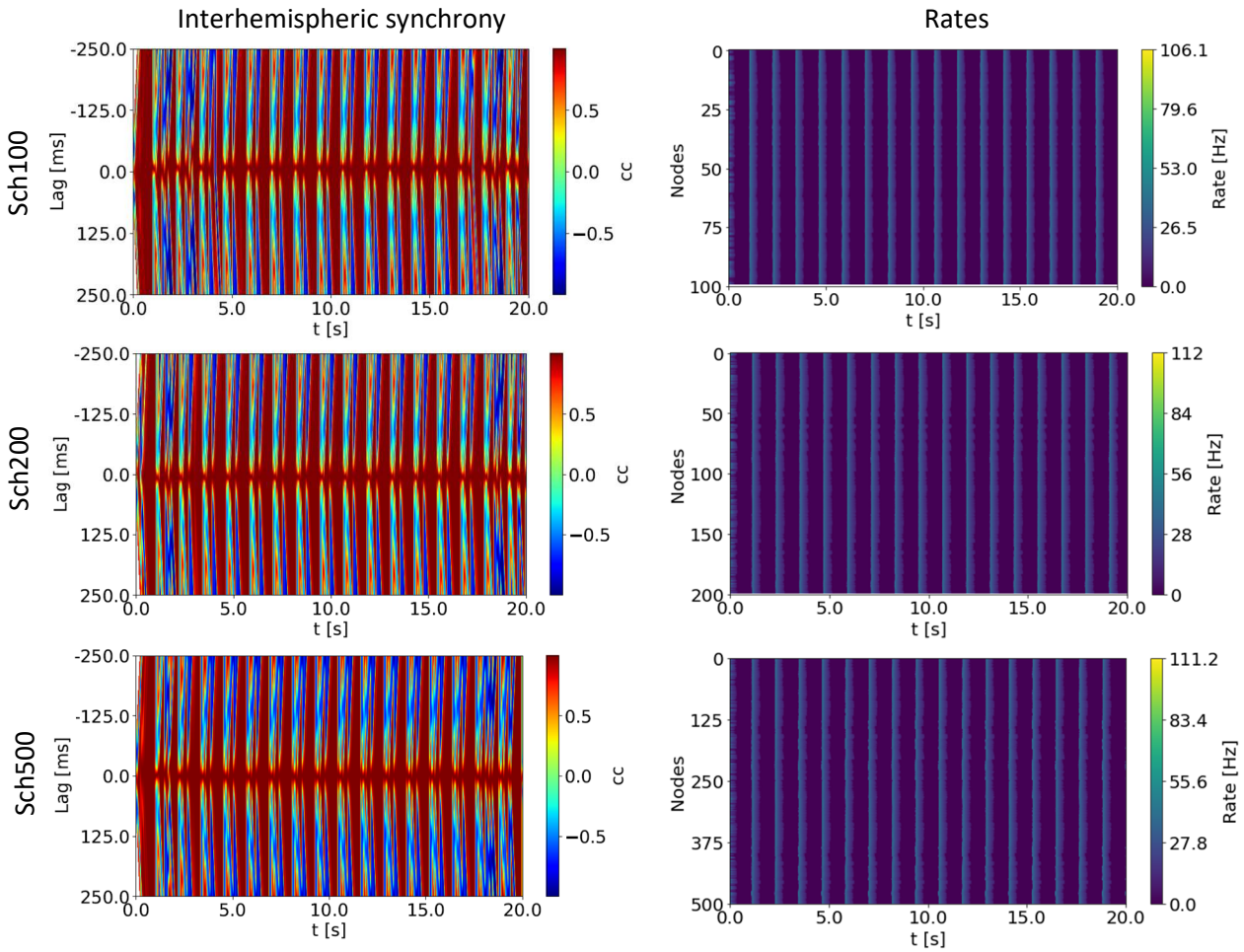

Figure 6: Spatiotemporal patterns with $\mu_E^{ext} = 2.5$ and $\mu_I^{ext} = 2.0$

On the other hand, when comparing the model's output with the empirical recordings, the FC matrix plots in Figure 7 show similar results for the different parcellations. Note that, in general, the simulated FC values are higher than the values in the empirical FC matrices, mainly because of the absence of noise when simulating. Nevertheless, as it can be observed in the matrices, the appearing connectivity patterns are more similar to the empirical functional connectivity the higher the resolution is. In Table 1 (first row), the values for the matrix correlations are shown (correlation between empirical FC and SC matrices and correlations between empirical and simulated FC matrices) and this better fit for higher resolutions is also reflected in the case of $(\mu_E^{ext}, \mu_I^{ext}) = (2.5,\ 2.0)$. A noticeable result is that for 500 nodes, the correlation value between simulated and empirical FC matrices is even higher than the correlation value for empirical FC and

SC matrices. This could indicate that empirical functional connectivity is better explained when simulating with parcellations of higher resolution.

The spatiotemporal analysis procedure was carried out for two other parameter points in the slow limit cycle with $(\mu_E^{ext}, \mu_I^{ext})$ = $(2.48,\ 1.84)$ and $(\mu_E^{ext}, \mu_I^{ext}) = (2.30, 1.75)$. While the outcomes for interhemispheric synchrony and firing rates were very similar to the plots in Figure 6 (see Supplementary Figure 3 and Supplementary Figure 5), the correlation values when comparing the simulated FC matrix o the empirical one showed different results (Supplementary Figure 4 and Supplementary Figure 6), which are also shown in Table 1. It can be seen that with $(\mu_E^{ext}, \mu_I^{ext})$ = $(2.48,\ 1.84)$, a point that is very close to the one analyzed before, a better fit to the empirical data is still reached when the granularity level is increased. Moreover, the correlation value for 500 nodes in the empirical versus simulated FC matrix is also higher than in the empirical SC-FC correlation. These higher correlation values are marked in bold font. However, when analyzing a parameter selection which is further away as $(\mu_E^{ext}, \mu_I^{ext}) = (2.30, 1.75)$, this relationship is no longer fulfilled. The correlation value between empirical and simulated FC matrices is increased when changing from 100 nodes to 200 nodes, but later, with 500 nodes, it slightly decreases again. Also, in this case, the correlation between empirical and simulated FC matrices is not over the correlation value between empirical FC and SC matrices for any level of resolution. This fact may indicate, that working with higher resolution levels can lead to better fitting, but only if the right parameter values are chosen. Therefore, in order to find the optimal parameter selection, an evolutionary optimization could be carried out, but this will remain out of this study.

Table 1: Empirical versus simulated FC matrix correlation comparison.

$(\boldsymbol{\mu_E^{ext}, \mu_I^{ext}})$	Empirical FC-SC corr.	Simulated FC – empirical FC corr.
$\boldsymbol{(2.5, 2.0)}$	Sch100: 0.33	Sch100: 0.14
	Sch200: 0.31	Sch200: 0.25
	Sch500: 0.27	**Sch500: 0.33**
$\boldsymbol{(2.48, 1.84)}$	Sch100: 0.33	Sch100: 0.11
	Sch200: 0.31	Sch200: 0.22
	Sch500: 0.27	**Sch500: 0.30**
$\boldsymbol{(2.30, 1.75)}$	Sch100: 0.33	Sch100: 0.15
	Sch200: 0.31	Sch200: 0.24
	Sch500: 0.27	Sch500: 0.23

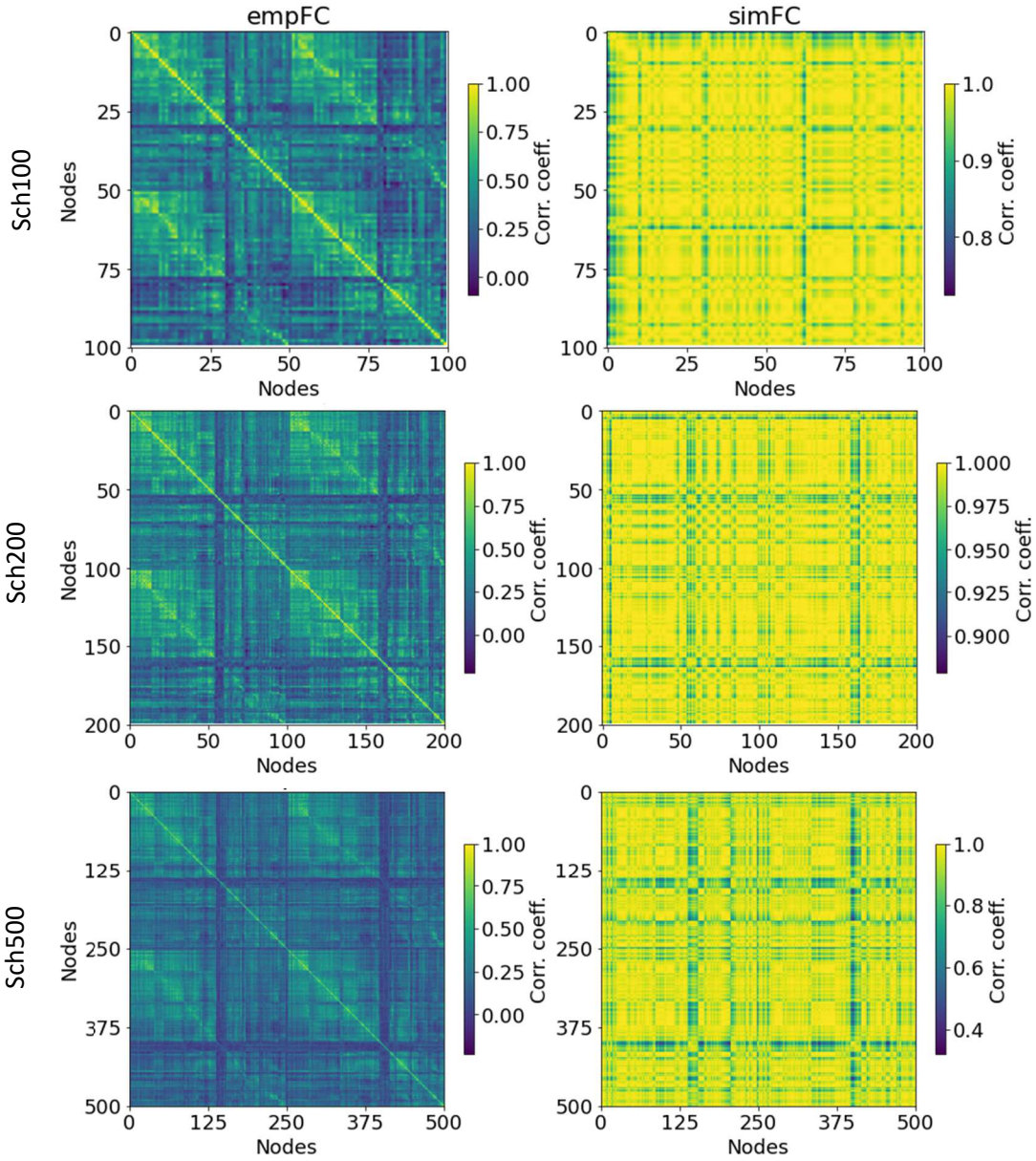

Figure 7: Comparison between empirical and simulated FC matrices with $\mu_E^{ext} = 2.5$ and $\mu_I^{ext} = 2.0$

5.3. Reproduced results from the work of Cakan et al. [9]

The following results are the reproduction of the different plots and statistics from the work of Cakan et al. [9], more specifically Figure 4. In this figure, SOs are reflected in the average firing rate plot as well as in the state time series, which lead to select one SO and analyze its propagation through the brain. Moreover, the given statistics describe the distribution of local and global phenomena as well as the ones from state durations. Additionally, it is shown how the node degree influences the time spent in each state and how the transition phase correlates with the node coordinates. All in all, this measures allow for a deep analysis of the sleep model in terms of local and global phenomena as well as wave propagation patterns. The statistics were computed on a 10 min simulation in [9] and this duration was also used in this study.

In order to reproduce the figures, three equivalent points to the one analyzed in [9] (one for each level of resolution) are selected via a small exploration around the original one (whose parameters are $\mu_E^{ext} = 3.3mV * ms^{-1}, \mu_I^{ext} = 3.7mV * ms^{-1}$, $b = 3.2pA, \tau_A = 4765ms$, $K_{gl} = 265, \sigma_{ou} = 0.37mV * ms^{-3/2}$). The equivalent points were obtained through a variation in b and τ_A (all other parameters remain constant) and are shown in Table 2. Several criteria were used to choose the equivalent points: the power spectra and the states plots. On the one hand, the power spectra of the three points were compared to the one of the point which is to reproduce from [9] (referred to as "AAL2") and to the empirical power spectrum. The results can be seen in Figure 8, which shows how in all cases, there is a higher frequency peak at around 1Hz, which is consistent with the frequency distribution of SOs.

Table 2: Parameter selection for the equivalent points.

	b	τ_A
Sch100	3.6 pA	4765 ms
Sch200	4.0 pA	4965 ms
Sch500	4.0 pA	4965 ms

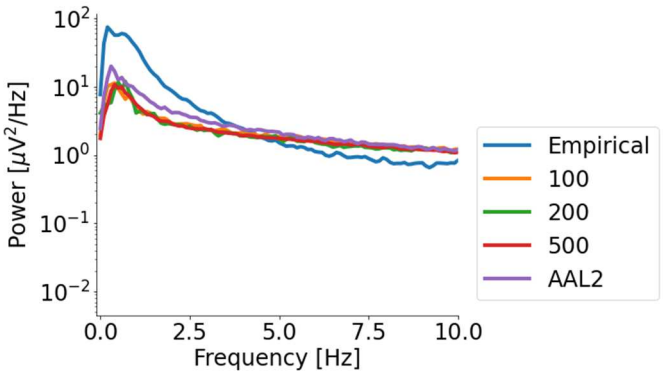

Figure 8: Comparison between power spectra.

On the other hand, the states plots (Figure 9) were compared to the ones in [9]. The results show similar plots, with more local than global phenomena and also some clearly marked global waves where almost all nodes are in the down-state at the same time. The latter can be observed as vertical blue lines. These results are put together with the average firing rate of all nodes (Figure 9), whose shape is reflected in the states plots as the peaks and valleys correspond with the global up- and down-states respectively. Note that this results are constant through the different granularity levels. However, it can be seen that, the higher the resolution is, the less noise is observed in the average rate plots, which could indicate a greater synchrony between the different nodes generating the signal.

Eventually, to check how the selected points fitted to the empirical data, the correlation between the simulated and the empirical FC matrixes was computed. The results (Table 3) show high correlation values between simulated and empirical FC matrices, which are also higher than the correlation values between empirical FC and SC matrices, meaning the selected points are a good fit to the empirical data. The plots of the comparison between empirical and simulated FC matrices for the equivalent points are added in the appendix (Supplementary Figure 7).

Table 3: Empirical versus simulated FC matrix correlation comparison for the equivalent points.

Parcellation Scheme	b	τ_A	Empirical FC-SC corr.	Simulated FC – empirical FC corr.
Sch100	3.6 pA	4765 ms	0.33	0.35
Sch200	4.0 pA	4965 ms	0.31	0.38
Sch500	4.0 pA	4965 ms	0.27	0.30

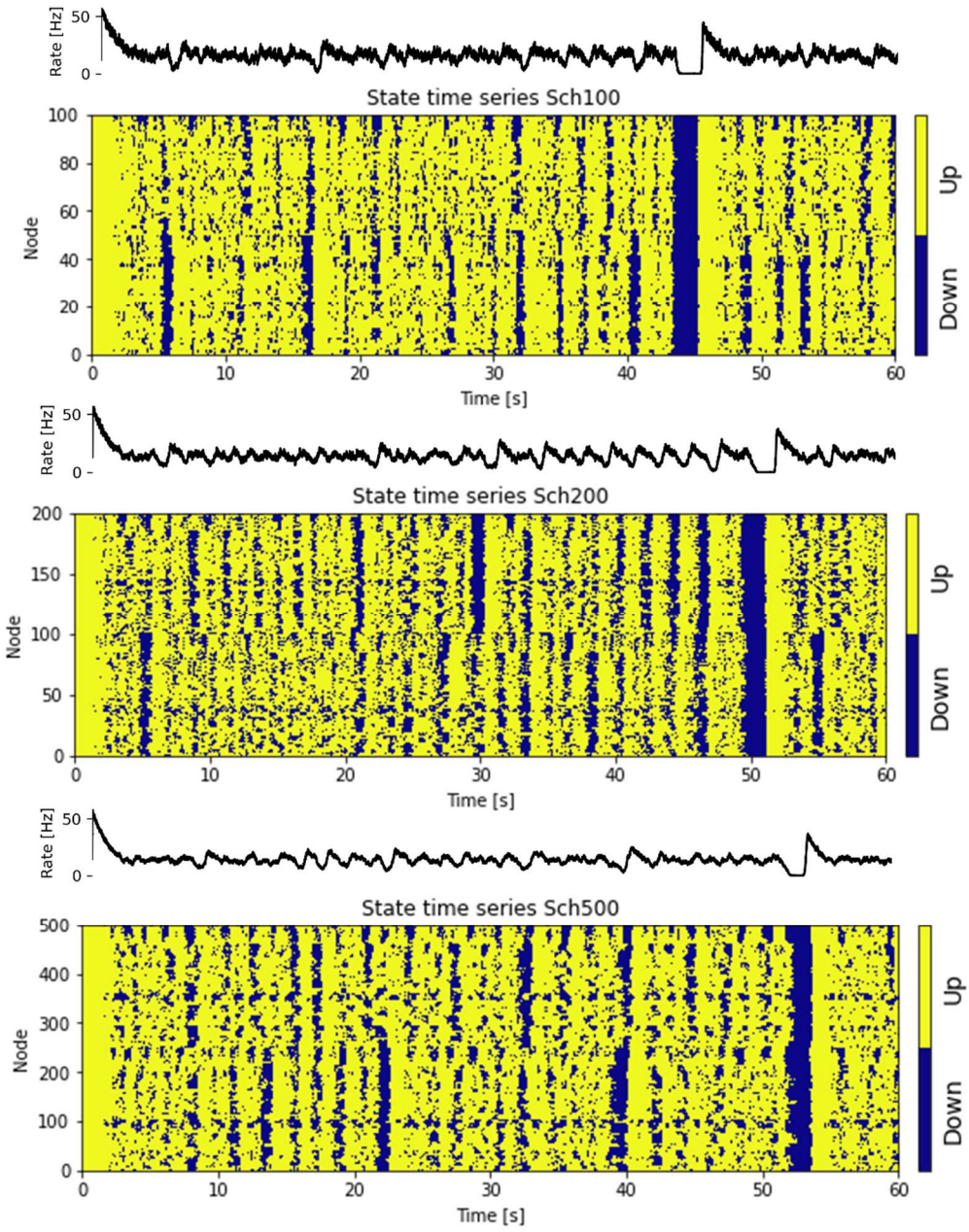

Figure 9: State plots and average firing rate for the equivalent points at different levels of resolution.

Furthermore, in order to observe whole-brain oscillations, in Figure 10, the wave propagation can be observed for the different selected points, for an interval of 1500. More concretely, this is the global wave observed in Figure 9. The results show how the SOs seem to start in the frontal right region and spread back and towards the left hemisphere. Depending on which nodes are the first transitioning again to the up-state, the network will jump again to the up-state starting in this region which will then propagate to the rest of the nodes. These results are corresponding to the ones in [9] in the fact that the silent wave seems to start in frontal regions (although with the Schaefer parcellation [7] it comes from the frontal right part concretely), but the return to the up-state is different in every case. The wave-propagation patterns will be examined in more detail in the statistics.

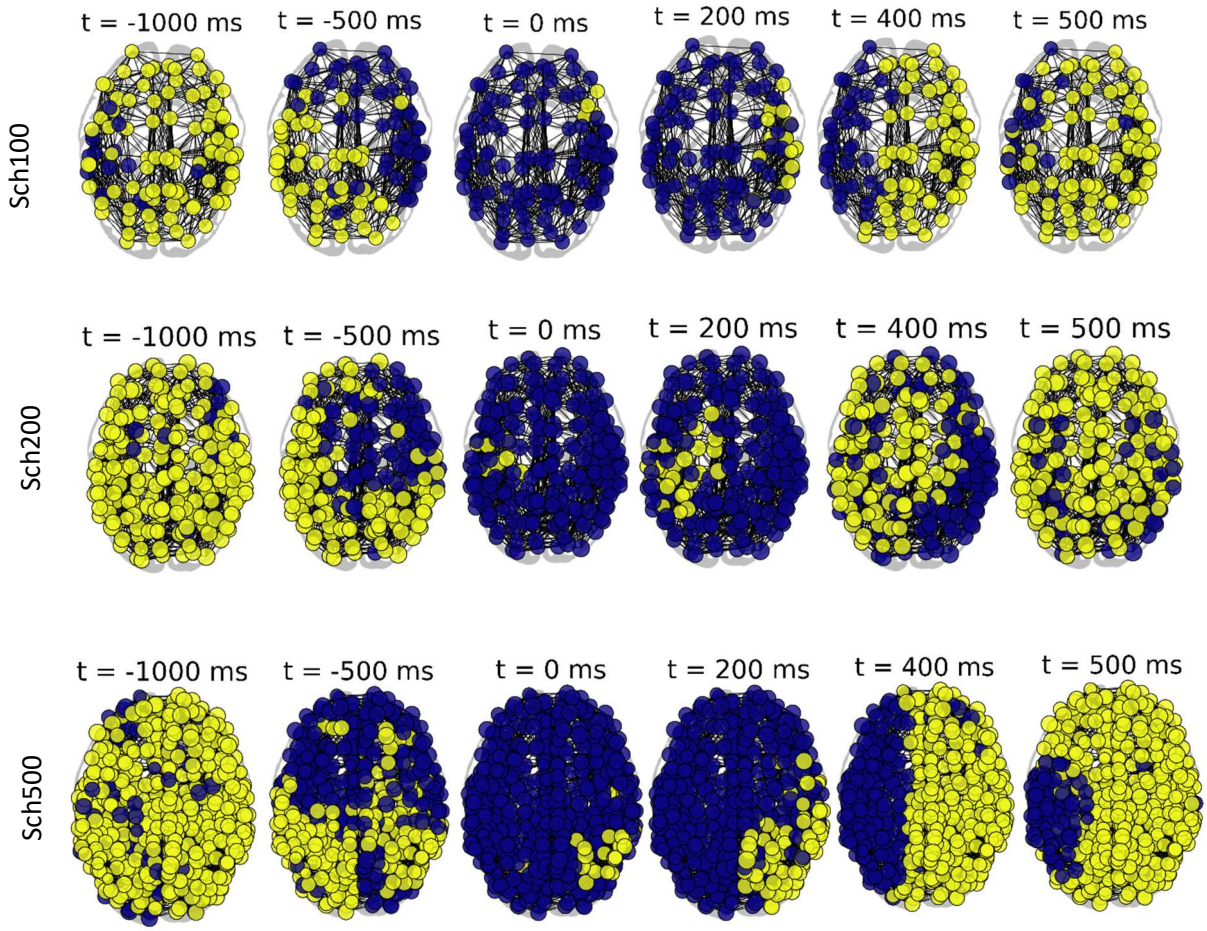

Figure 10: Wave propagation thorough the different levels of resolution

Coming to the statistical analysis, firstly, up- and down-state durations are exponentially distributed for all levels of resolution (Figure 12 A), similar to [9]. In general, up-states last longer than down-states. These results are consistent with the ones obtained empirically [30]. Regarding the distribution of the down-state involvement (Figure 12 B), it can be seen that most phenomena are local, as the proportion of nodes simultaneously taking part in the down-state shows lower values. This distribution remains as described for all parcellations and is also reflected in [9] and in

human intracranial recordings [32]. In addition, when analyzing the inter-event interval for local and global oscillations (Figure 11 C), the plots show how local phenomena occur more frequently (shorter inter-event interval) than global ones. This happens for 100, 200 and 500 nodes, as well as in [9] and it can also be observed experimentally [33]. The next plots (Figure 11 D) show how, for all levels of resolution, down-states last longer when more brain areas are involved. The reason for this is that adjacent regions receive less input the more areas are in the down-state. Nevertheless, in the case of the up-state duration, it can be seen how duration values are increased with the involvement until it reaches around 65%, when greater adaptation inhibitory currents appear due to the high firing rates and the up-state duration is shortened again. This can be observed with 100, 500 nodes and in [9], but not as clear in the case of 200 nodes. Continuing with the relationship between firing rate and involvement (Figure 11 E), all parcellations show a proportional relationship between both of them, meaning that, the more regions are in the up-state, the higher the average firing rates of SOs are [9]. Eventually, the relationship between the node degree and the time spent in each state (Figure 11 F) highlights how nodes with higher degree (i.e. higher connectivity to other nodes) spend more time in the up-state (and therefore less time in the down-state) as they receive stronger inputs from other regions. This relationship is shown for all levels of resolution as well as in [9].

The statistical measurements analyzed until this point were all consistent throughout the levels of resolution and with the results from [9], however, when it comes to travelling wave patterns, the obtained outcome differs from the one in the work of Cakan et al.. Regarding the relationship between state transition phases and node coordinates (in [9] Figure 4 L) there is a strong correlation between up-to-down and down-to-up transition phases and the coordinates of the brain areas, whereas here (Figure 12 A), this correlation does not appear at any level of resolution. Also, the down state duration values (Figure 12 B) are higher in the middle part and not in the front (as shown in [9] Figure 4 I). In addition, the values of the transition phases (Figure 12 C) are firstly, not as spread (in a smaller interval) and not homogeneous in the frontal areas (as in [9] Figure 4 K). All these results are not consistent with the theory that SOs travel in a preferred direction from anterior to posterior regions. The suggested reason why these results differ from the ones in [9] is the degree distribution. Note that in the AAL2 parcellation [29], there is a strong correlation between the node degree and their coordinates in the y-axis (i.e. from anterior to posterior areas), meaning that the nodes in the frontal regions have lower degree values. Therefore, the nodes in the frontal areas receive less inputs and are therefore more likely to be responsible for starting SOs as waves of silence. Nevertheless, in the Schaefer parcellation [6], this relationship is no longer true, or at least not as evident as in the AAL2 parcellation [29]. The node degree and the coordinates in the y-axis show linear correlation (Figure 12 D), but with lower values than in AAL2 as shown in Figure 13 taken from [9] and Table 4. Also, the degree distribution from the AAL2 [29] and Schaefer parcellation [6] differ from each other in the fact that the AAL2 parcellation [29] contains more nodes with lower degree values and the distribution is in general wider than in the Schaefer parcellation [7], where degree values are not that spread and the distributions are therefore narrower. This can be seen in Figure 14.

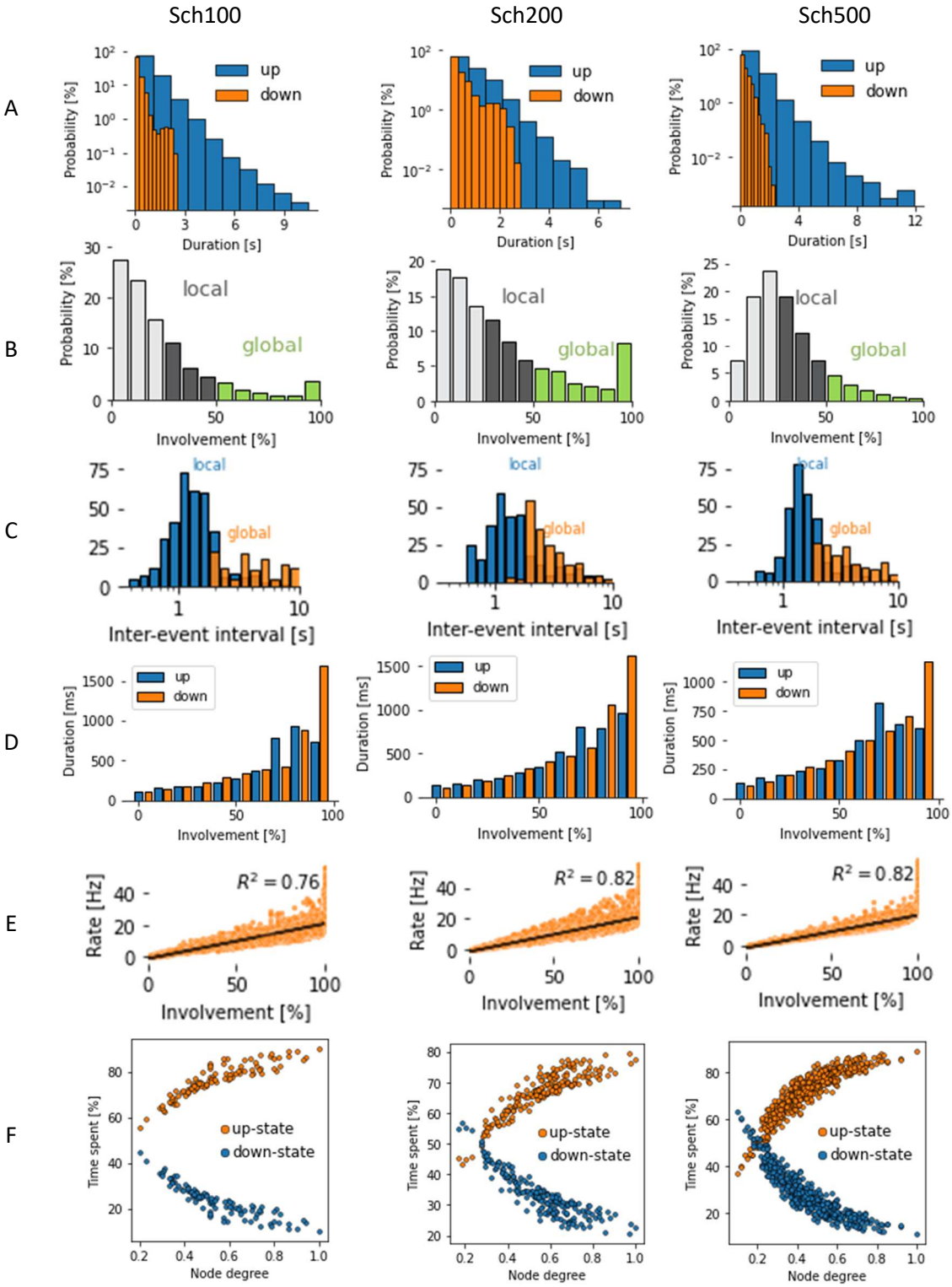

Figure 11: Statistical measures from the 10 min simulation

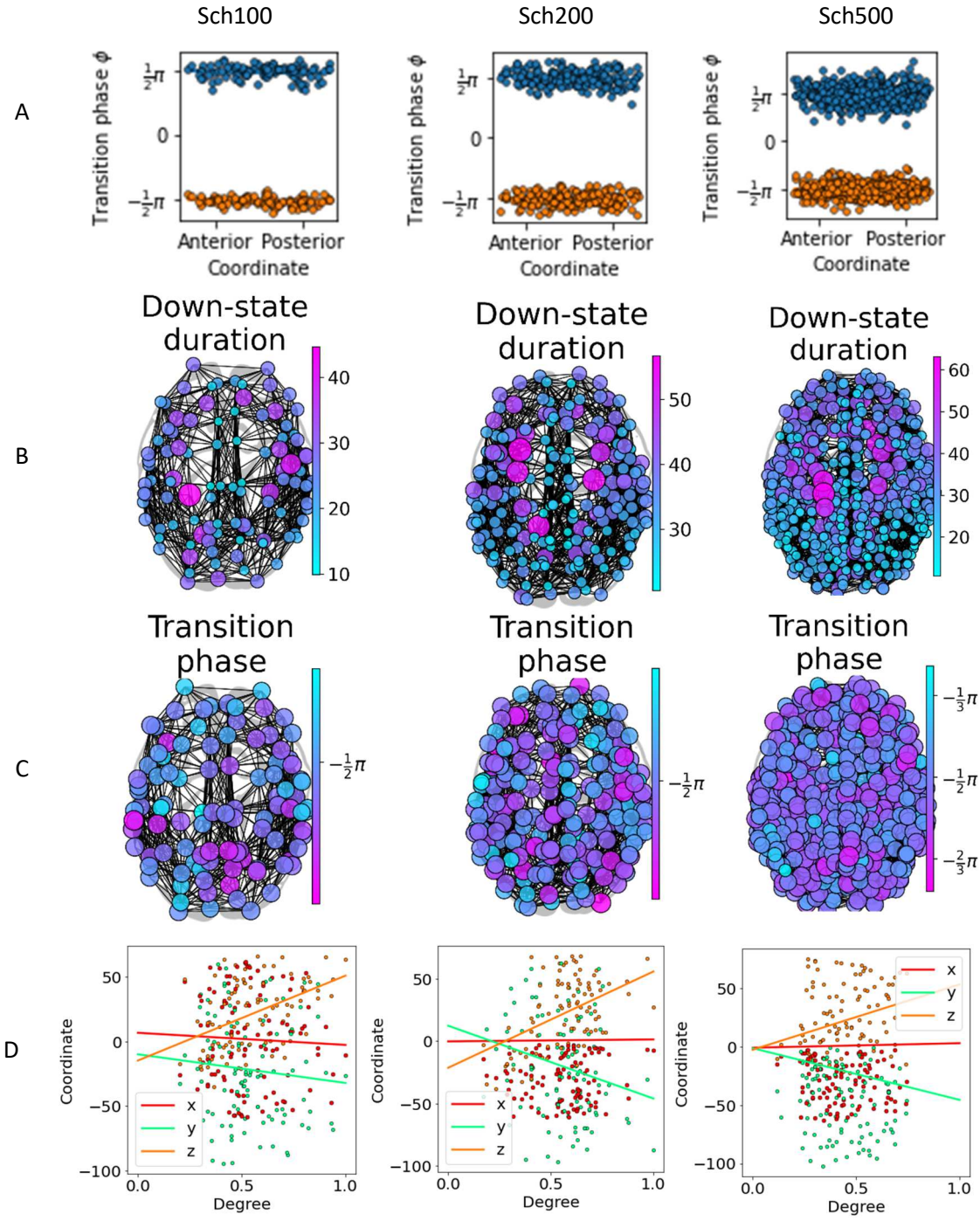

Figure 12: Statistical measures of wave propagation patterns from the 10 min simulation

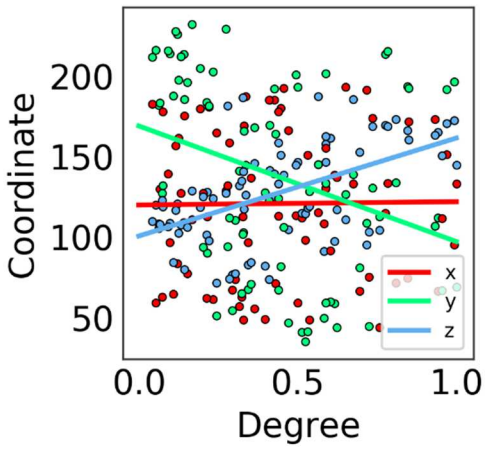

Figure 13: Node degree and node coordinates correlation from the work of Cakan et al. [9]

Table 4: Linear regression values between node degree and coordinates.

	AAL2			Sch100			Sch200			Sch500		
	Slope	r-value	p-value	Slope	r-value	p-value	Slope	r-value	p-value	Slope	r-value	p-value
X	2.02	0.01	0.92	-9.38	-0.04	0.66	1.56	0.01	0.92	3.88	0.02	0.71
Y	-71.81	-0.32	0.004	-22.21	-0.09	0.34	-58.47	-0.24	0.001	-44.32	-0.18	8.76
z	60.87	0.53	4.12	65.79	0.43	6.85	77.38	0.44	6.41	55.94	0.31	3.09

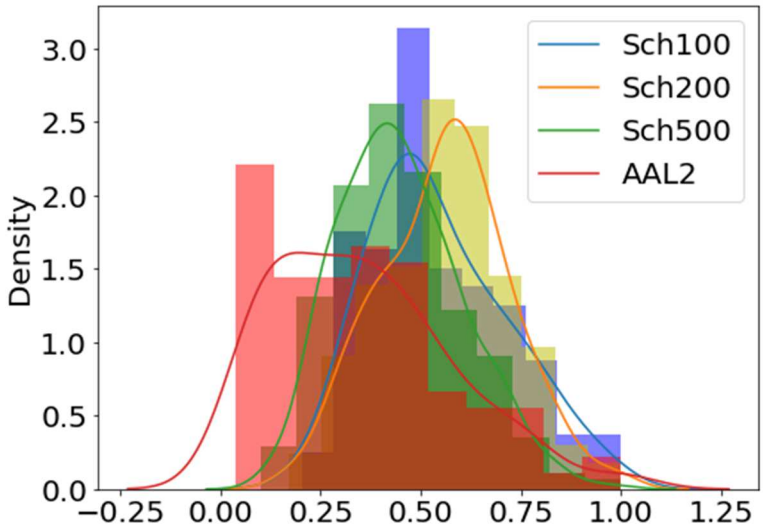

Figure 14: Degree distributions (Kernel densities and histograms)

6. DISCUSSION AND CONCLUSIONS

Computational whole-brain models are an innovative and useful technique to analyze and gain a deeper understanding of complex brain dynamics. In this field, the implementation of neural mass models serves to reduce dimensionality of the system and allows for suitable and more efficient simulations. Following this idea, when modelling the brain as a network of connected nodes which represent single brain areas composed of larger neuron populations, the choice of the brain parcellation can influence the output of the model.

In this work, an analysis has been carried out in order to check whether the increase in regional resolution has an impact in the results of a deep sleep whole-brain model, particularly focusing in SOs. Regional granularity is an important factor, as connections between human brain areas are less than 50mm apart, but there is no consensus about the regional level of resolution when simulating and analyzing SOs. Therefore, the goal of this study was to explore whether there are significant differences in the appearing spatiotemporal patterns when the level of granularity is increased. To this aim, different aspects of the behavior of the model have been examined.

Firstly, it has been proven that the state space of the model is not influenced by the usage of a different parcellation scheme, nor by the increase of the number of nodes (Figure 5). Also, for the examined points, the appearing spatiotemporal patterns remained almost constant across the different levels of resolution (Figure 6). A potential explanation for the lack of differences in the interhemispheric synchrony which should also be investigated in future work is the fact that SOs propagate from anterior to posterior regions, rather than in lateral direction. These very similar results across all granularity levels are favorable in sense of computational efficiency, as working with lower levels of resolutions is considerably faster. However, there were signs that working with a higher parcellation resolution could explain a larger portion of empirical functional connectivity patterns, if the optimal parameter space was chosen (Table 1). This is a significant result, because of the importance of the connectome in brain dynamics, especially in SOs, which are shown to be guided by it [4]. For this reason, in order to analyze SOs through whole-brain modelling, a good fitting to the connectivity data is required and this aspect can be improved through higher resolution parcellations at expense of time and computational resources.

On the other hand, many statistical measures show constant distributions across the different levels of granularity (Figure 11) showing that, in general, there are more local than global oscillatory phenomena and their durations are homogeneously distributed for all levels of resolution. SOs can be observed with every parcellation scheme and show similar patterns in terms of frequency and involvement, but the origin of where the SOs are generated is not clear in this study. Other work as [9] show consistent results with the theory that SOs spread from anterior to posterior regions, but the results obtained here are diverse. Other studies such as [34] (where different source modelling methods were used to identify the origin of SOs) also concluded that there seems to be heterogeneity in the origin of SOs. Here, they established that qualitatively, the average sleep SO probably begins in anterior regions and spreads back afterwards, but each particular spontaneous wave showed different propagation patterns [34]. Therefore, future work should also try to quantify the origin of SOs in order to clarify this aspect.

The suggested reason for the appearing differences in the wave propagation patterns is the node connectivity distribution (reflected in the node degree measures, Figure 14). SOs simulated with parcellations with a lower node degree in the frontal areas (such as the AAL2 used in [9]) do indeed emerge in frontal areas, as these nodes receive less input from their neighbors and are therefore more likely to remain silent. However, when the degree distribution changes, this rule is no longer fulfilled. This fact is shown in the current results with the Schaefer parcellation [7], where the node degree has a narrower distribution with higher node degree values in general (also in the frontal regions). Given these results, another suggestion for future lines of research is to examine the role of the node degree distribution in the dynamics of SOs. Therefore, the node degree could be manipulated manually and the effects on the wave travelling patterns could be examined.

It should also be noted that the chosen points for reproducing the results from [9] when substituting the parcellations scheme in this study show a reasonably good fit to the empirical data in terms of simulated and empirical FC matrix correlation, as the obtained correlation values are between 0.3 and 0.38 (Table 3). However, given the fact that the correlations are lower than in [9], where the best score was 0.56 when adaptation was considered, it would be warranted to run an evolutionary optimization with the new parcellation to check whether other parameter configuration could yield a higher fit.

All in all, this study shows how the choice of parcellation resolution can be a crucial aspect when dealing with computational whole-brain models, specifically in the case of studying SOs, and should therefore be taken into account not only for simulating but also when it comes to analyze the results and compare them to the work of others. One more time, the importance of the node connection degree distribution should be noted. Hence, it should be obtained in a way that the brain networks are reproduced as closely as possible, in order to obtain results that are realistic and representative.

7. BIBLIOGRAPHY

[1] B. Rasch and J. Born, "About Sleep's Role in Memory," *Physiol. Rev.*, vol. 93, no. 2, pp. 681–766, Apr. 2013, doi: 10.1152/physrev.00032.2012.

[2] C. Cakan, N. Jajcay, and K. Obermayer, "neurolib: a simulation framework for whole-brain neural mass modeling." bioRxiv, p. 2021.02.18.431886, Feb. 18, 2021. doi: 10.1101/2021.02.18.431886.

[3] K. J. Friston, A. Mechelli, R. Turner, and C. J. Price, "Nonlinear Responses in fMRI: The Balloon Model, Volterra Kernels, and Other Hemodynamics," *NeuroImage*, vol. 12, no. 4, pp. 466–477, Oct. 2000, doi: 10.1006/nimg.2000.0630.

[4] C. Cakan, C. Dimulescu, L. Khakimova, D. Obst, A. Flöel, and K. Obermayer, *Criticality and the role of the connectome in shaping slow oscillations in the brain during deep sleep*. 2020.

[5] D. J. Ardesch, L. H. Scholtens, and M. P. van den Heuvel, "Chapter 6 - The human connectome from an evolutionary perspective," in *Progress in Brain Research*, vol. 250, M. A. Hofman, Ed. Elsevier, 2019, pp. 129–151. doi: 10.1016/bs.pbr.2019.05.004.

[6] M. Rubinov and O. Sporns, "Complex network measures of brain connectivity: uses and interpretations," *NeuroImage*, vol. 52, no. 3, pp. 1059–1069, Sep. 2010, doi: 10.1016/j.neuroimage.2009.10.003.

[7] A. Schaefer *et al.*, "Local-Global Parcellation of the Human Cerebral Cortex from Intrinsic Functional Connectivity MRI," *Cereb. Cortex N. Y. N 1991*, vol. 28, no. 9, pp. 3095–3114, Sep. 2018, doi: 10.1093/cercor/bhx179.

[8] J. A. Roberts *et al.*, "Metastable brain waves," *Nat. Commun.*, vol. 10, no. 1, Art. no. 1, Mar. 2019, doi: 10.1038/s41467-019-08999-0.

[9] "Frontiers | Spatiotemporal Patterns of Adaptation-Induced Slow Oscillations in a Whole-Brain Model of Slow-Wave Sleep | Frontiers in Computational Neuroscience." https://www.frontiersin.org/articles/10.3389/fncom.2021.800101/full (accessed May 26, 2022).

[10] O. V. Popovych *et al.*, "Inter-subject and inter-parcellation variability of resting-state whole-brain dynamical modeling," *NeuroImage*, vol. 236, p. 118201, Aug. 2021, doi: 10.1016/j.neuroimage.2021.118201.

[11] P. Peigneux *et al.*, "Are spatial memories strengthened in the human hippocampus during slow wave sleep?," *Neuron*, vol. 44, no. 3, pp. 535–545, Oct. 2004, doi: 10.1016/j.neuron.2004.10.007.

[12] M. Mölle, L. Marshall, S. Gais, and J. Born, "Learning increases human electroencephalographic coherence during subsequent slow sleep oscillations," *Proc. Natl. Acad. Sci. U. S. A.*, vol. 101, no. 38, pp. 13963–13968, Sep. 2004, doi: 10.1073/pnas.0402820101.

[13] M. W. Woolrich *et al.*, "Bayesian analysis of neuroimaging data in FSL," *NeuroImage*, vol. 45, no. 1 Suppl, pp. S173-186, Mar. 2009, doi: 10.1016/j.neuroimage.2008.10.055.

[14] T. E. J. Behrens *et al.*, "Non-invasive mapping of connections between human thalamus and cortex using diffusion imaging," *Nat. Neurosci.*, vol. 6, no. 7, pp. 750–757, Jul. 2003, doi: 10.1038/nn1075.

[15] J. H. Kaas, "The Organization of Neocortex in Mammals: Implications for Theories of Brain Function," *Annu. Rev. Psychol.*, vol. 38, no. 1, pp. 129–151, 1987, doi: 10.1146/annurev.ps.38.020187.001021.

[16] C. Capaday, C. Ethier, warren Darling, and C. Van Vreeswijk, "On the functional organization and operational principles of the motor cortex," *Front. Neural Circuits*, vol. 7, 2013, Accessed: May 25, 2022. [Online]. Available: https://www.frontiersin.org/article/10.3389/fncir.2013.00066

[17] R. L. Buckner and B. T. T. Yeo, "Borders, Map Clusters, and Supra-Areal Organization in Visual Cortex," *NeuroImage*, vol. 93, no. Pt 2, pp. 292–297, Jun. 2014, doi: 10.1016/j.neuroimage.2013.12.036.

[18] R. L. Buckner and F. M. Krienen, "The evolution of distributed association networks in the human brain," *Trends Cogn. Sci.*, vol. 17, no. 12, pp. 648–665, Dec. 2013, doi: 10.1016/j.tics.2013.09.017.

[19] A. L. Cohen *et al.*, "Defining functional areas in individual human brains using resting functional connectivity MRI," *NeuroImage*, vol. 41, no. 1, pp. 45–57, May 2008, doi: 10.1016/j.neuroimage.2008.01.066.

[20] M. van den Heuvel, R. Mandl, and H. Hulshoff Pol, "Normalized cut group clustering of resting-state FMRI data," *PloS One*, vol. 3, no. 4, p. e2001, Apr. 2008, doi: 10.1371/journal.pone.0002001.

[21] "Generation and Evaluation of a Cortical Area Parcellation from Resting-State Correlations | Cerebral Cortex | Oxford Academic." https://academic.oup.com/cercor/article/26/1/288/2367115 (accessed May 25, 2022).

[22] S. B. Eickhoff, B. Thirion, G. Varoquaux, and D. Bzdok, "Connectivity-based parcellation: Critique and implications," *Hum. Brain Mapp.*, vol. 36, no. 12, pp. 4771–4792, Dec. 2015, doi: 10.1002/hbm.22933.

[23] G. Deco, V. K. Jirsa, P. A. Robinson, M. Breakspear, and K. Friston, "The Dynamic Brain: From Spiking Neurons to Neural Masses and Cortical Fields," *PLOS Comput. Biol.*, vol. 4, no. 8, p. e1000092, Aug. 2008, doi: 10.1371/journal.pcbi.1000092.

[24] H. Huang, "Mechanisms of dimensionality reduction and decorrelation in deep neural networks," *Phys. Rev. E*, vol. 98, no. 6, p. 062313, Dec. 2018, doi: 10.1103/PhysRevE.98.062313.

[25] C. Cakan and K. Obermayer, "Biophysically grounded mean-field models of neural populations under electrical stimulation," *PLOS Comput. Biol.*, vol. 16, no. 4, p. e1007822, Apr. 2020, doi: 10.1371/journal.pcbi.1007822.

[26] R. Jolivet, R. Kobayashi, A. Rauch, R. Naud, S. Shinomoto, and W. Gerstner, "A benchmark test for a quantitative assessment of simple neuron models," *J. Neurosci. Methods*, vol. 169, no. 2, pp. 417–424, Apr. 2008, doi: 10.1016/j.jneumeth.2007.11.006.

[27] R. Brette and W. Gerstner, "Adaptive Exponential Integrate-and-Fire Model as an Effective Description of Neuronal Activity," *J. Neurophysiol.*, vol. 94, no. 5, pp. 3637–3642, Nov. 2005, doi: 10.1152/jn.00686.2005.

[28] M. Augustin, J. Ladenbauer, F. Baumann, and K. Obermayer, "Low-dimensional spike rate models derived from networks of adaptive integrate-and-fire neurons: Comparison and implementation," *PLOS Comput. Biol.*, vol. 13, no. 6, p. e1005545, Jun. 2017, doi: 10.1371/journal.pcbi.1005545.

[29] E. T. Rolls, M. Joliot, and N. Tzourio-Mazoyer, "Implementation of a new parcellation of the orbitofrontal cortex in the automated anatomical labeling atlas," *NeuroImage*, vol. 122, pp. 1–5, Nov. 2015, doi: 10.1016/j.neuroimage.2015.07.075.

[30] T.-A. E. Nghiem *et al.*, "Cholinergic Switch between Two Types of Slow Waves in Cerebral Cortex," *Cereb. Cortex N. Y. N 1991*, vol. 30, no. 6, pp. 3451–3466, May 2020, doi: 10.1093/cercor/bhz320.

[31] "The Asynchronous State in Cortical Circuits." https://www.science.org/doi/10.1126/science.1179850 (accessed Jul. 04, 2022).

[32] Y. Nir *et al.*, "Regional slow waves and spindles in human sleep," *Neuron*, vol. 70, no. 1, pp. 153–169, Apr. 2011, doi: 10.1016/j.neuron.2011.02.043.

[33] J. Kim, T. Gulati, and K. Ganguly, "Competing Roles of Slow Oscillations and Delta Waves in Memory Consolidation versus Forgetting," *Cell*, vol. 179, no. 2, pp. 514-526.e13, Oct. 2019, doi: 10.1016/j.cell.2019.08.040.

[34] "Source modeling sleep slow waves | PNAS." https://www.pnas.org/doi/10.1073/pnas.0807933106 (accessed Jul. 13, 2022).

APPENDIX

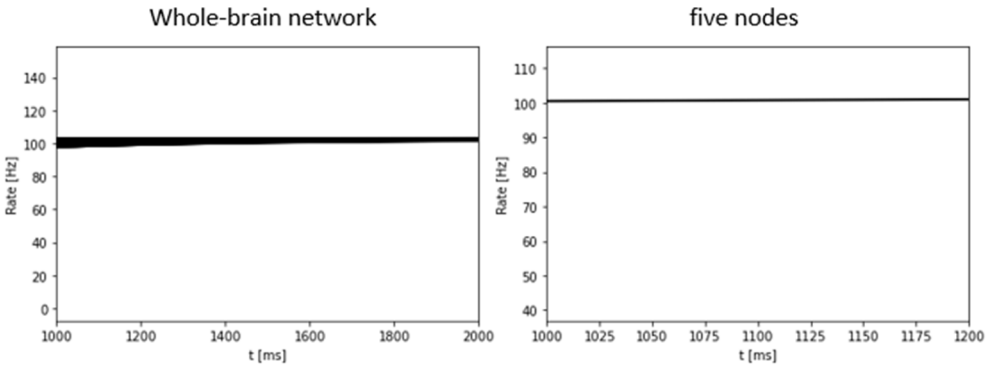

Supplementary Figure 1: Firing rates from the network in the artifact region with $\mu_E^{ext} = 4$ and $\mu_I^{ext} = 0.5$

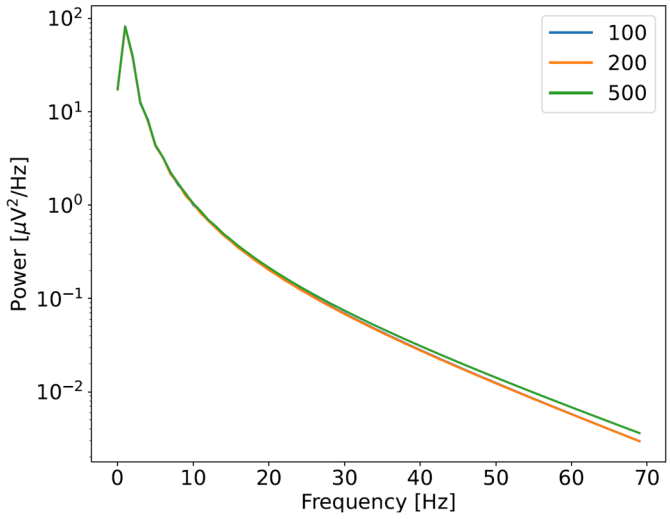

Supplementary Figure 2: Power spectra for the different levels of resolution of the selected point in the spatiotemporal analysis

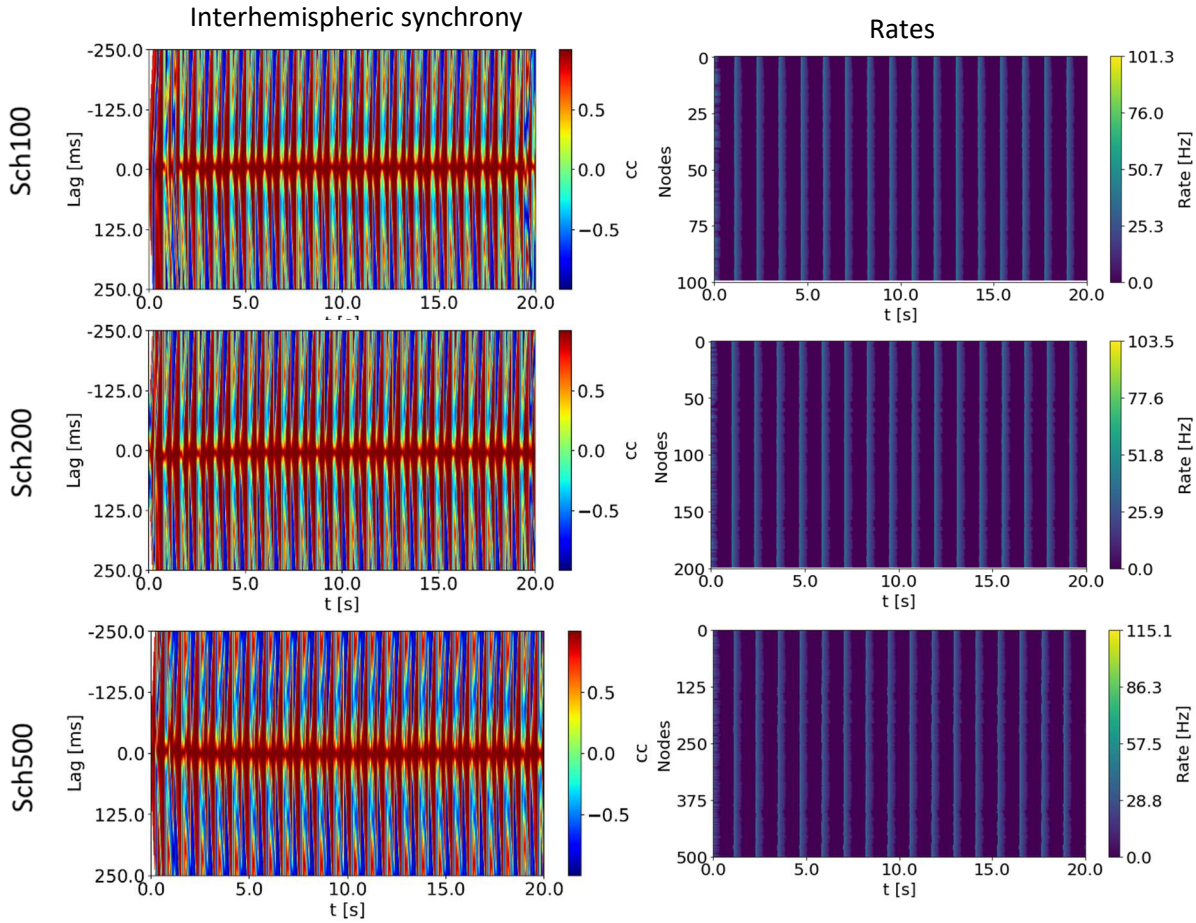

Supplementary Figure 3: Spatiotemporal patterns with $\mu_E^{ext} = 2.48$ and $\mu_I^{ext} = 1.84$

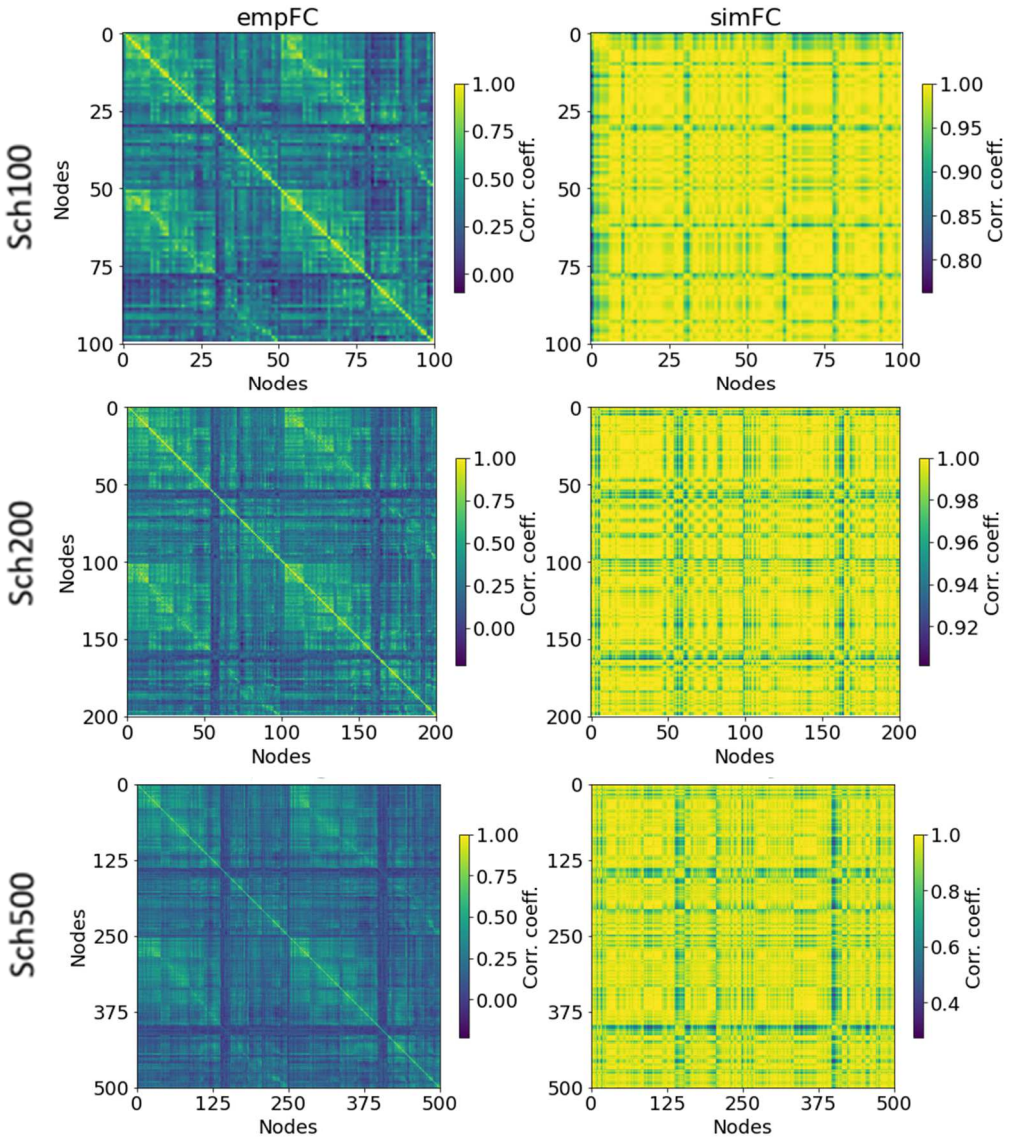

Supplementary Figure 4: Comparison between empirical and simulated FC matrices with $\mu_E^{ext} = 2.48$ and $\mu_I^{ext} = 1.84$

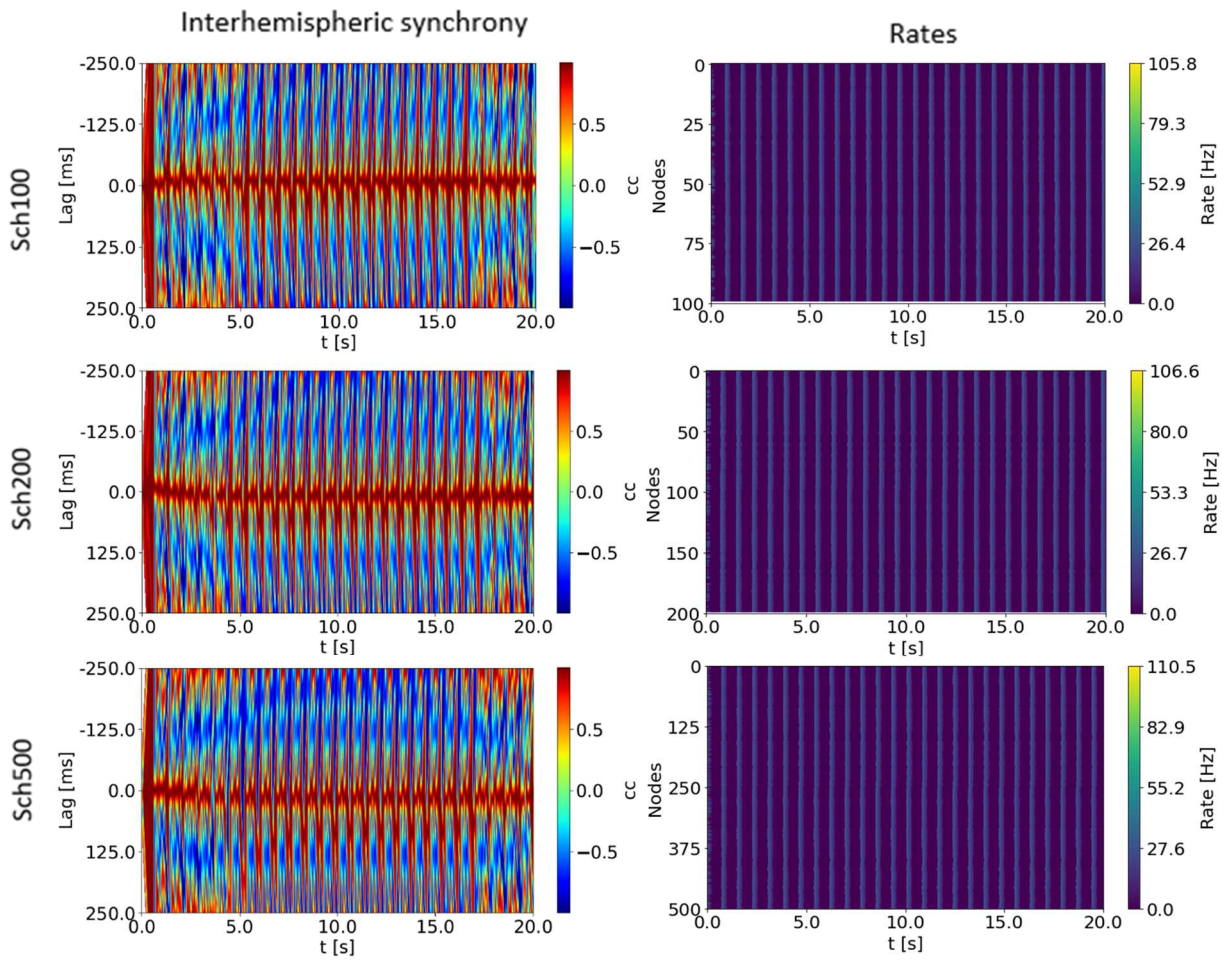

Supplementary Figure 5: Spatiotemporal patterns with $\mu_E^{ext} = 2.3$ and $\mu_I^{ext} = 1.75$

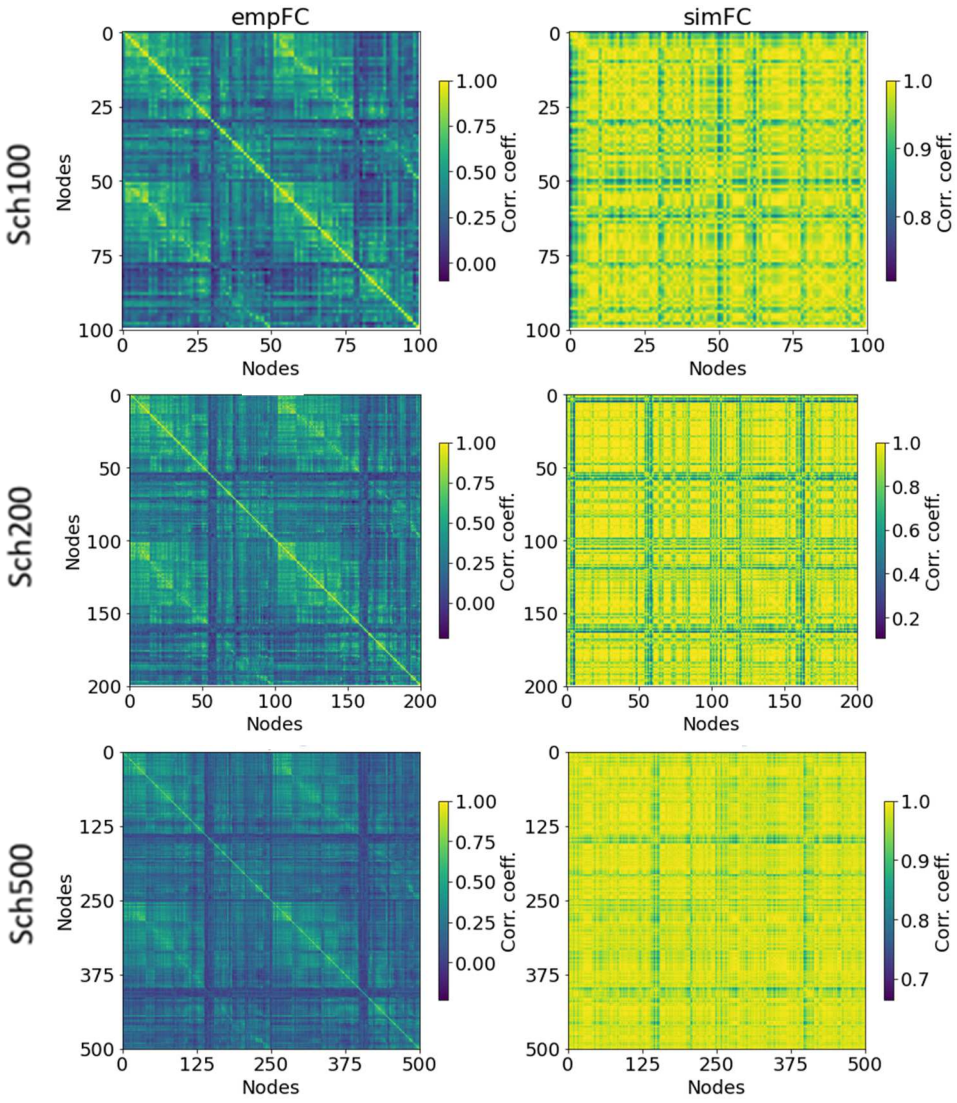

Supplementary Figure 6: Comparison between empirical and simulated FC matrices with $\mu_E^{ext} = 2.3$ and $\mu_I^{ext} = 1.75$

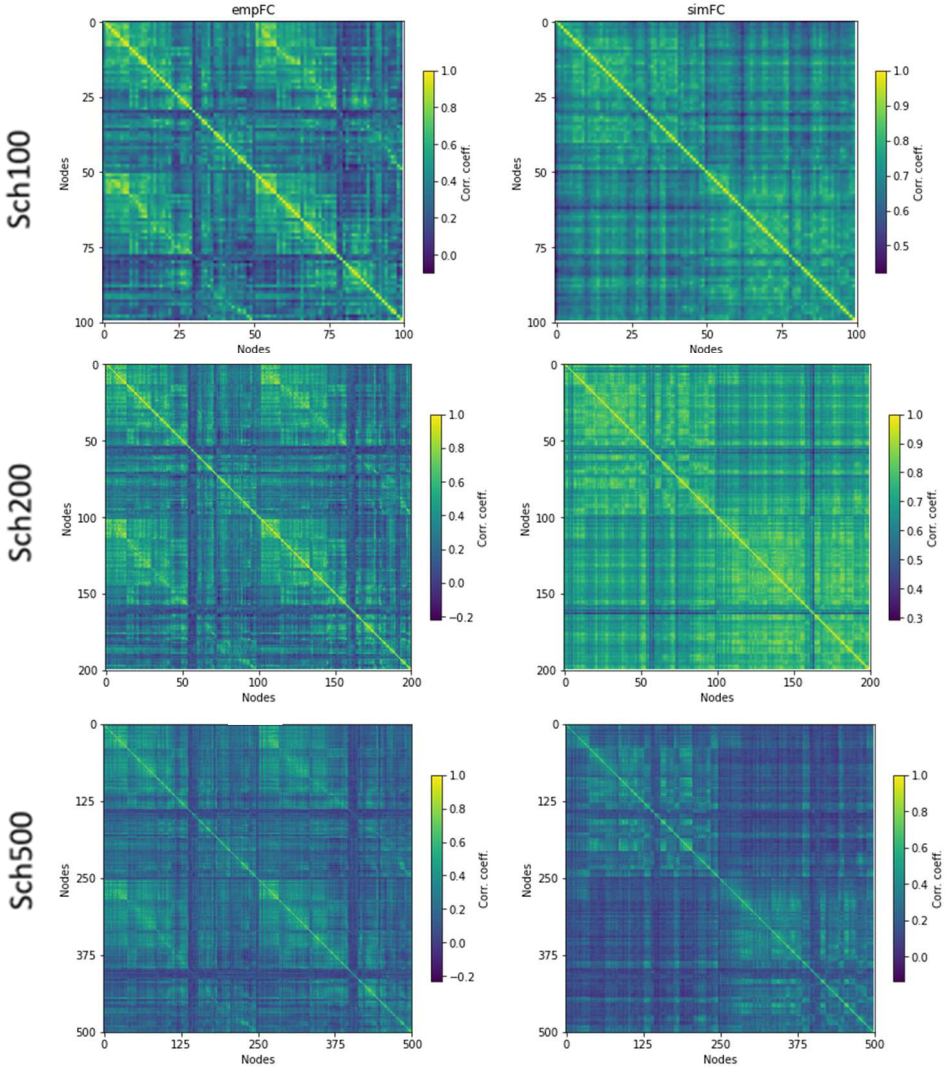

Supplementary Figure 7: Comparison of empirical and simulated FC matrices of the three equivalent points chosen for the reproduction of the statistic in [9]